



Numerical simulation of convective heat transfer coefficients at the external surfaces of building arrays immersed in a turbulent boundary layer

Jiying Liu^a, Jelena Srebric^{b,*}, Nanyang Yu^a

^aSchool of Mechanical Engineering, Southwest Jiaotong University, Chengdu 610031, China

^bDepartment of Architectural Engineering, The Pennsylvania State University, University Park, PA 16802, USA

ARTICLE INFO

Article history:

Received 7 July 2012

Received in revised form 29 January 2013

Accepted 1 February 2013

Keywords:

Convective heat transfer coefficients

Plan area density

Building energy consumption

Numerical simulation

ABSTRACT

The convective heat transfer is an important component in the total energy balance for arrays of buildings immersed in a turbulent boundary layer. This study examines convective heat transfer coefficients (CHTC) at the external windward, leeward, lateral and top surfaces of buildings. This study uses Large Eddy Simulations (LES) with Smagorinsky–Lilly model to predict CHTC and then compares the simulation results with experimental data. In addition, steady RANS including the realizable $k-\varepsilon$ and the shear stress transport $k-\omega$ turbulence models are also validated with the experimental data. However, both of these RANS models overestimated CHTC values for arrays of buildings in contrast to LES predictions. Regular arrays of cubic buildings are modeled to investigate CHTC in an urban environment, which are arranged according to different plan area densities ($\lambda_p = 0.44, 0.25, 0.16, 0.11, 0.063$ and 0.04). This morphological parameter (λ_p) represents different urban neighborhoods and it is used to characterize different flow regimes in an urban environment. The CHTC distributions are independent of the Reynolds number based on different incoming wind velocities at a height of 10 m above the ground (U_{10}) for windward, leeward, lateral and top building surfaces. Furthermore, CHTC distributions for different λ_p and $U_{10} = 5$ m/s are compared with flow characteristics in building arrays. Finally, the CHTC correlations as a function of λ_p and U_{10} were obtained, where λ_p varies from 0.04 to 0.25 and the Reynolds number ranges from 7×10^5 to 5×10^6 . With the increase of the plan area densities from 0.04 to 0.25, CHTCs increases 15% for the leeward surface and decreases 16% for the lateral surfaces. Consequently, a total energy balance and the energy consumption predictions for a building need to take into account the urban density of the building surroundings.

© 2013 Elsevier Ltd. All rights reserved.

1. Introduction

The convective heat transfer coefficients (CHTC) on external surfaces of a building are crucial parameters for accurate evaluations of building thermal performance and associated building energy consumption [1]. Several studies have demonstrated that the simulated energy consumption can vary from 20% to 40% due to different choices of CHTC values for internal building surfaces [2–4]. In addition, another study has also shown that an uncertainty of 15% for CHTC at external building surfaces can result in a corresponding uncertainty of 20% in heat flux calculations throughout the envelope [5]. Furthermore, for external surfaces, the overall heat flux sensitivity to CHTC is even greater because the outdoor surface velocities are equal or much greater than the indoor surface velocities. For example, CHTCs are especially relevant to studies on solar collectors [6], green roofs [7] and urban heat island mitigation strategies [8]. CHTC is also an important parameter in

the total energy balance for a building in an urban environment, especially when the building enclosure materials have a relatively low thermal resistance, resulting in a relatively high sensitivity of the total energy balance to CHTCs [9]. In summary, accurate predictions of CHTCs enable accurate calculations of the heat losses or gains for an external building surface.

To obtain better predictions of the CHTC at the external surfaces of buildings, a large number of studies have been carried out by means of wind-tunnel experiments [10–12], numerical simulations [9,13–16] and field measurements [17–22]. In all of these studies, CHTCs were correlated to the reference mean wind speed at a height of 10 m above the ground with the incoming wind profiles typically defined as logarithmic or power-law correlations. The influences of the wind direction have also been studied by developing different CHTCs for windward and leeward surfaces. However, the majority of the existing studies were limited to a building roof and/or vertical walls of a single isolated building, or to a certain location of a single building surface.

Existing CHTCs are not suitable for a deployment to an entire neighborhood of buildings due to the complex building geometries

* Corresponding author. Tel.: +1 814 863 2041; fax: +1 814 863 4789.

E-mail address: jsrebric@engr.psu.edu (J. Srebric).

and airflow patterns that are not all accounted for in the previous studies. Nevertheless, the existing CHTC correlations are a good starting point to develop a comprehensive set of correlations for applications to an actual urban neighborhood. A recent study performed by Saneinejad et al. [23] showed that numerical simulations were able to predict the CHTCs in the windward and leeward walls of a street canyon. The study analyzed the spatial variation of CHTC in 2D urban areas. However, the accuracy of the simulation results was limited due to the flow limitations to upward and downward directions in 2D urban canyons, which differs from an actual 3D urban area [24]. Furthermore, Narita [25] developed a water evaporation technique to study the distribution of convective heat transfer coefficients in urban environments. However, 2D street canyon models were still employed. Both studies gave a general recommendation that the use of 3D building models is needed.

It should be noted that wind played a significant role in predicting existing correlations for the CHTC, which can also be strongly impacted by the buildings' surroundings. In an urban environment, a building's surroundings create a shelter effect that can reduce local wind speeds. This sheltering effect has been first taken into consideration in building infiltration studies [26–28]. More recently, Lovely et al. [18] presented the concept of sheltering effects when predicting the CHTCs for external building surfaces. This study provided an important contribution although it primarily focused on the angle of wind incidence affecting the values of CHTCs for windward or leeward building surfaces.

Despite complex vortex and flows in urban area, the morphological parameters, such as the building plan area density (λ_p) and frontal area density (λ_f), have been shown to be important in predicting urban airflow patterns [29]. Additionally, the values of surface roughness height (z_0) in many meteorological and wind-engineering problems, especially in regular obstacle arrays, is an important factor in modeling environmental wind effects [30]. Therefore, when estimating the CHTC values at the external surfaces for arrays of cubes representing buildings immersed in a turbulent boundary layer, taking into account the morphological parameters and features of the atmospheric boundary layer is necessary.

In this paper, Computational Fluid Dynamics (CFD) based on Reynolds-Averaged Navier–Stokes (RANS) equations and Large Eddy Simulation (LES) with the Smagorinsky–Lily subgrid model are firstly carried out to predict CHTCs in a 3D cubic array. Comparisons against wind tunnel experimental results reveal the predictive accuracy of currently used models. As a relatively more accurate simulation method, LES is then used to simulate flow field for the regular arrays of buildings and calculate the CHTCs for windward surfaces, leeward surfaces, lateral surfaces and rooftops, with different cube layouts defined by six different plan area densities ($\lambda_p = 0.44, 0.25, 0.16, 0.11, 0.063$ and 0.04).

2. Governing equations and turbulence models

In the present study, the realizable k – ε turbulence model [31] and the shear stress transport (SST) k – ω turbulence model [32] are applied with RANS to simulate CHTCs for external surfaces of buildings. In addition to these two RANS models, LES with Smagorinsky–Lily model [33] is also used to validate the simulation results with experimental data.

2.1. Reynolds-Averaged Navier–Stokes model

The governing equations of continuity, momentum and energy for steady incompressible flows and heat transfer with negligible radiation and buoyancy effects are expressed as follows:

$$\frac{\partial u_i}{\partial x_i} = 0 \quad (1)$$

$$\frac{\partial (u_i u_j)}{\partial x_j} = -\frac{1}{\rho} \frac{\partial p}{\partial x_j} + \frac{\partial}{\partial x_j} \left(\mu \left(\frac{\partial u_i}{\partial x_j} + \frac{\partial u_j}{\partial x_i} \right) - \overline{u_i u_j} \right) \quad (2)$$

$$\frac{\partial (u_i T)}{\partial x_i} = \frac{1}{\rho c_p} \frac{\partial}{\partial x_i} \left(\lambda \frac{\partial T}{\partial x_i} \right) + \frac{\partial}{\partial x_j} \left(-\overline{u_j T} \right) \quad (3)$$

where $-\overline{u_i u_j}$ is the Reynolds stress tensor, and $-\overline{u_j T}$ is the turbulent heat flux. By relating the stress tensor and turbulent heat flux to the mean strain-rate and mean temperature gradients, respectively, the two unknowns can be solved as follows:

$$-\rho \overline{u_i u_j} = \mu_t \left(\frac{\partial u_i}{\partial x_j} + \frac{\partial u_j}{\partial x_i} \right) - \frac{2}{3} \rho \delta_{ij} k \quad (4)$$

$$-\rho c_p \overline{u_j T} = q_c = \lambda_t \frac{\partial T}{\partial z} \quad (5)$$

where μ_t is the turbulent dynamic viscosity, λ_t is the turbulent thermal conductivity ($\lambda_t = C_p \mu_t / Pr_t$), which is proportional to μ_t since the turbulent Prandtl number, Pr_t , ranges from 0.7 to 0.9 depending on the laminar Prandtl number of the fluid [34]. For the two used RANS turbulence models, μ_t is related to the turbulent kinetic energy (k) and turbulent dissipation rate (ε) or the specific dissipation rate (ω). As a consequence, in order to solve Eq. (4) and (5), two additional closure equations are required to enable the computation of the Reynolds stress tensor and turbulent heat fluxes.

More details about the two transport equations and corresponding parameter settings for both the realizable k – ε turbulence model and the SST k – ω turbulence model can be found in Shih et al. [31] and Menter [32]. For the former model, near-wall treatment is taken into consideration for the viscous sublayer, which in other words is a low-Reynolds number model, used instead of the wall functions. This enhanced wall treatment is a near-wall modeling method that employs the one-equation model of Wolfshtein [35] to resolve the viscosity-affected in the near wall region, in which the turbulent Reynolds number, $Re^* = \rho y k^{1/2} / \mu$, is smaller than 200. Accordingly, the dimensionless wall distance, $y^+ = \rho u^* y / \mu$, at the wall-adjacent cell should be on the order of $y^+ \approx 1$. The SST k – ω turbulence model itself is available as the low-Reynolds number model, which treats the wall boundary condition in the same way as the enhanced wall treatments [36]. In that case, a smaller y^+ value at the wall-adjacent cell ($y^+ \approx 1$) is also required.

2.2. Large Eddy Simulation

In LES, the continuity, momentum and energy equations for incompressible flows and heat transfer are filtered as follows:

$$\frac{\partial \bar{u}_i}{\partial x_i} = 0 \quad (6)$$

$$\frac{\partial \bar{u}_i}{\partial t} + \frac{\partial (\bar{u}_i \bar{u}_j)}{\partial x_j} = -\frac{1}{\rho} \frac{\partial \bar{p}}{\partial x_i} + \nu \frac{\partial^2 \bar{u}_i}{\partial x_i \partial x_j} - \frac{\partial \tau_{ij}}{\partial x_j} \quad (7)$$

$$\frac{\partial \bar{T}}{\partial t} + \frac{\partial (\bar{u}_j \bar{T})}{\partial x_j} = \frac{\nu}{Pr} \frac{\partial^2 \bar{T}}{\partial x_i \partial x_j} - \frac{\partial h_j}{\partial x_j} \quad (8)$$

where $\tau_{ij} = \overline{u_i u_j} - \bar{u}_i \bar{u}_j$ and $h_j = \overline{u_j T} - \bar{u}_j \bar{T}$ are the subgrid-scale stress tensor and subgrid-scale heat flux, respectively. Both of them are unresolved and need to be modeled. Therefore, the Smagorinsky–Lily subgrid model is applied. In this model, the subgrid-scale tensor with the eddy viscosity hypothesis is given as:

$$\tau_{ij} - \frac{1}{3} \tau_{kk} \delta_{ij} = \nu_{sgs} \left(\frac{\partial \bar{u}_i}{\partial x_j} + \frac{\partial \bar{u}_j}{\partial x_i} \right) = -2 \nu_{sgs} \bar{S}_{ij} \quad (9)$$

and where ν_{sgs} is the subgrid-scale eddy viscosity defined by:

$$\nu_{sgs} = (C_S \bar{\Delta})^2 |\bar{S}| \quad (10)$$

here, C_S is the Smagorinsky constant, $\bar{\Delta}$ is $(\bar{\Delta}_1 \bar{\Delta}_2 \bar{\Delta}_3)^{1/3}$, in which $\bar{\Delta}_j$ ($j = 1, 2, 3$) is specified as the spatial grid size in the j direction, $|\bar{S}|$ is the resolved strain-rate tensor given by $|\bar{S}| = (2\bar{S}_{ij}\bar{S}_{ij})^{1/2}$.

The subgrid-scale heat flux, h_j , is modeled by the subgrid-scale eddy diffusivity (α_t) hypothesis with constant subgrid-scale Prandtl number, Pr_t , as follows:

$$h_j = -\alpha_t \frac{\partial \bar{T}}{\partial x_j} = -\frac{\nu_{sgs}}{Pr_t} \frac{\partial \bar{T}}{\partial x_j} \quad (11)$$

The following constants have been used in this Smagorinsky–Lily subgrid model: $C_S = 0.1$, $Pr_t = 0.85$. Further, the near-wall treatment uses the proposed analytical integration of power-law near-wall velocity distribution based on the work of Werner and Wengle [37].

3. CFD Validation

A critical step in the use of CFD for numerical studies is its validation with measured data. In this present study, an experiment with arrays of cubes was used to validate CFD simulations. This section first describes the experiment setup, and then presents the numerical models, including the computational domain, grid distribution, boundary conditions, and discretization scheme. In the last part of this section, detailed comparisons between CFD results and experimental data demonstrate the model accuracy.

3.1. Description of experiment

The CFD validation is conducted with the experimental data available in Meinders et al. [38]. This wind tunnel had a rectangular test section with the height of 500 mm and width of 50 mm. An array of nine identical cubes, with their side dimensions of 15 mm, was placed at half of the vertical channel height. The aspect ratio (W/H) between the spacing of two streamwise cubes to the cube height was set to 1. The schematic of this experimental configuration is given in Fig. 1. These cubes were made of an internal copper core of 12 mm in length covered with an epoxy layer of 1.5 mm thickness. An infrared camera was used to measure exterior surface temperature distribution of the epoxy layer and then to calculate local and overall surface convective heat transfer. All cubes were heated at the copper core temperature of 75 °C. The thermal conductivity of the epoxy layer is approximately 0.24 W/m K. This experiment was performed with the bulk velocity of 5.1 m/s, resulting in a Reynolds number of approximately 5065 based on

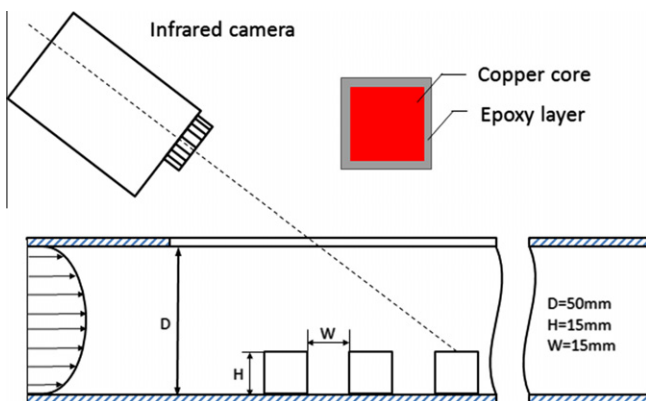


Fig. 1. Schematic of experimental configuration and measurement cube.

the cube height. The approaching airflow temperature was set to 21 °C, which was also taken as the reference temperature to calculate the CHTCs. Additional details about this experiment setup and data acquired can be found in the literatures [38,39].

3.2. Numerical model

The computational domain replicated the actual experiment setup, except for the length of the domain, which was established based on the guideline by Franke et al. [40]. For this fully developed turbulent flow, the computational domain included a length of 5 times the cube height (5H) upstream of the first cube, and 15H downstream of the last cube. Fig. 2 shows the computational domain specified for the CFD validation. A structured grid was used in the computational domain, with a refined grid in the vicinity of the cubes' exterior surfaces as shown in Fig. 3. Compared to the high Reynolds turbulence models, where a wall function can be used, the selected low Reynolds turbulence model requires a smaller y^+ value ($y^+ \approx 1$), which is also taken into account by the LES. Therefore, both LES and the low Reynolds turbulence model have the same grid distribution adjacent to cubes' surfaces. It should be noted that the grid requirements for LES and RANS are different, although the numbers of structured cells (7235,600) for each of the two computational domains were the same in this study. In addition, an average cell size in the wake between two cubes is $0.0005 \text{ m} \times 0.0005 \text{ m} \times 0.0005 \text{ m}$ (length \times width \times height) approximately. Grid sensitivity test was conducted to ensure the computational accuracy for LES simulations, and the same grid was used for RANS assuming grid independence based on LES results. The grid refinement ratio for three-dimensional mesh was defined as the ratio between the number of grid elements in the fine and coarse meshes “ r ”. Roache [41] showed that $r = 1.1$ is a sufficient refinement ratio for simple meshes. Therefore, this study used $r = 1.2$ to ensure sufficiently large grid refinement ratio. Three different grid distributions in the wake between two cubes were arranged with $42 \times 42 \times 42$ (coarse mesh, Δ_1), $50 \times 50 \times 50$ (medium, Δ_2) and $60 \times 60 \times 60$ (fine, Δ_3) using structured elements. For different grid distributions, the surface-averaged skin friction coefficient (C_f) for the windward surface of the fifth cube was compared. This quantitative grid verification was performed using the grid convergence index (GCI) [42] based on Richardson extrapolation [40]. In this study, the GCI was described as $GCI[\text{fine}] = F_S |\epsilon| / (r^p - 1)$, where $F_S = 1.25$ is the safety factor when comparing three grids, ϵ is the relative error between coarse and fine grid solutions and $p = 2$ represents the second-order method. The results showed that $GCI[3,2] = 2.05\%$, and $GCI[2,1] = 5.12\%$. It was found that a low value of GCI occurred between medium grid and fine grid. The grid distribution of $50 \times 50 \times 50$ shows a good performance resulting in a grid independent flow around cubes. Therefore, this grid distribution was adopted in between all cubes.

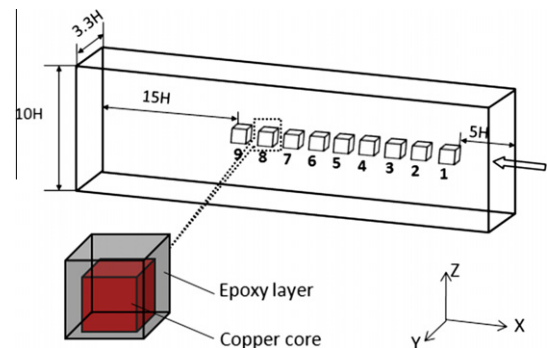


Fig. 2. The computational domain for validation case.

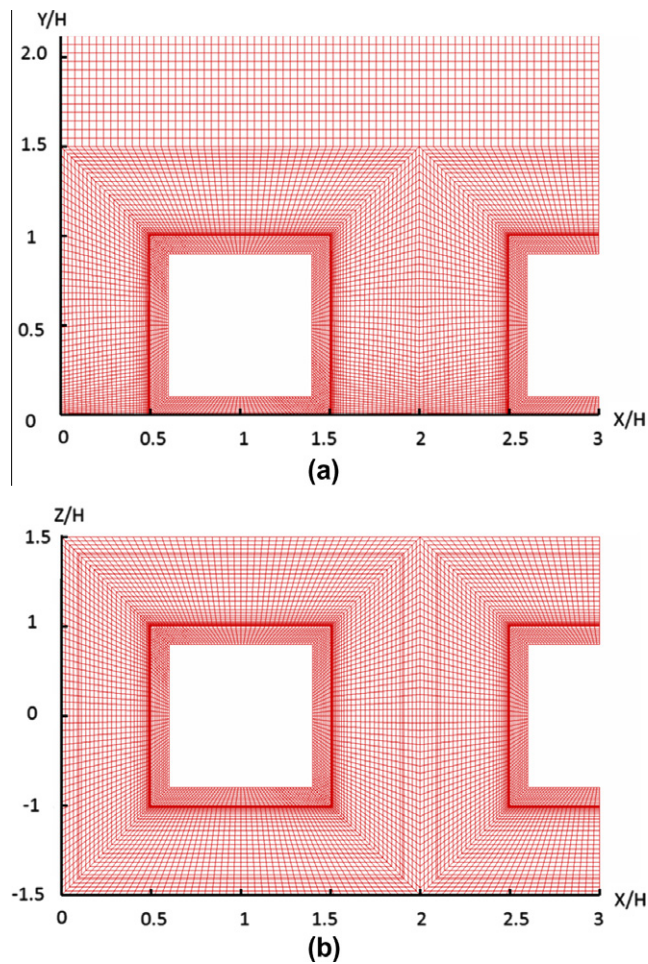


Fig. 3. Grid distributions around one cube in X–Y plane and in Z–X plane.

The spatial discretization error was also estimated by means of Richardson extrapolation [40,42], and it is about 2% for the Skin friction coefficient (C_f) of the windward surface for the fifth cube. A uniform temperature of 75 °C was specified in the copper core of the cubes. A coupled boundary was applied at the epoxy layer. The physical properties used in the simulations are presented in Table 1. The exterior cube surfaces were specified as no-slip boundaries with zero roughness. For the ground boundary of the domain, no-slip boundary conditions and adiabatic surface were assumed. Zero static pressure at the outlet and no-slip boundary conditions at the top and lateral boundaries were also specified. The bulk velocity, $U_{bulk} = 5.1$ m/s and uniform temperature, $T = 21$ °C were specified at the domain inlet. Due to typically limited availability of inlet boundary conditions in the literature [39], a two-dimensional simulation of an empty, perfectly smooth domain was suggested as a way to generate inlet turbulence intensity in the absence of experimental data [15]. The turbulence intensity obtained from this two-dimensional case was then adopted for the inlet boundary conditions in the non-empty simulation

Table 1
Physical properties of air and epoxy layer.

	Air	Epoxy layer
Density (kg/m ³)	1.225	1668
Specific heat capacity (J/kg K)	1006.4	1150
Thermal conductivity (W/m K)	0.0257	0.24
Viscosity (kg/m s)	2.197×10^{-5}	–

domain. After adopting the turbulence intensity, the simulated surface-averaged CHTC value at the windward surface of the leading cube was compared with the experimental data. A good agreement was obtained after several trials. Then, the generated final inlet turbulence intensity was assumed to be an accurate approximation of boundary conditions for numerical simulations when experimental data are not available. For LES, time dependent boundary conditions were required at the inlet. Several previous studies on airflow around wall-mounted cubes have demonstrated that the vortex method can be imposed to generate a time-dependent velocity profile with LES [43–45]. The number of vortices $N = 190$, therefore, was used to represent the inlet boundary conditions in LES computations. In this study, the CFD simulations were conducted using the control volume method with Ansys Fluent12.0 [36]. For the RANS simulations, the second-order upwind discretization scheme was used for the convective and diffusion terms, and SIMPLE algorithm was used for the pressure–velocity coupling. The spatial discretization for momentum and energy are both second-order upwind. The pressure was interpolated by a second order scheme. For LES, the convective term was discretized by the second-order central-differencing scheme. The pressure was interpolated by a second order scheme. The spatial discretization for the momentum and energy equations uses the second-order upwind scheme. Furthermore, in LES, the PISO scheme was imposed for pressure–velocity coupling method with the Skewness-Neighbor coupling. The time-dependent terms were interpolated by the implicit second-order interpolation scheme. The time step is set to $\Delta t = 0.0001$ s,

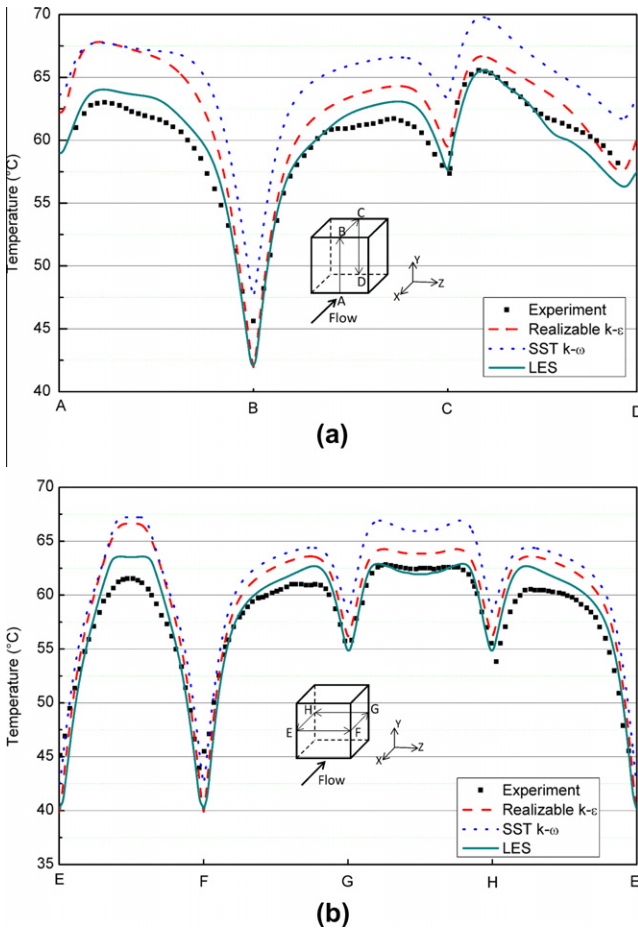


Fig. 4. Temperature distributions on the surface around the fifth cube along path (a) ABCD in the vertical plane and (b) the path EFGH in the horizontal plane (b).

which ensures that Courant–Friedrichs–Levy (CFL) number ($CFL = u\Delta t/\Delta x$, where u is the local velocity magnitude and Δx is the local grid size) is always smaller than 1 in most of the grid points, with a maximal value of 2.0. The time period $5T$ ($T = L/U_{10}$, where L is the domain size) and $10T$ is used to remove the influence of the initial condition and provide the time-averaged data.

3.3. Validation results

For the validation purposes, detailed measured data are compared to the simulation results around the fifth cube, which is in the middle of the cube array. Fig. 4 presents the validation results for the temperature distributions in the vertical and horizontal planes at the surfaces of the fifth cube. The simulated temperatures by the SST $k-\omega$ turbulence model exhibit larger overall discrepancies of up to 15% when compared to the performance of other simulation results. The average difference between experimental data and results obtained with the SST $k-\omega$ turbulence model in the windward, leeward and top surfaces is approximately 10%.

The realizable $k-\varepsilon$ turbulence model with the one-equation Wolfshtein model shows slightly better simulation results that have a better agreement with the experimental data than those obtained with the SST $k-\omega$ turbulence model. The worst agreement with the experimental data shows an overestimation for local temperatures of more than 10% at the windward surface. This discrepancy could be attributed to the inaccurate predictions of flow field for separation and reattachment around the first two cubes resulting in a prediction of larger temperature values further downstream. Although

many studies [9,14,15] have demonstrated that this low Reynolds model can predict the windward surface for an isolated cube immersed in a turbulent boundary layer, slight discrepancy obtained for leeward surfaces and considerable discrepancies observed for top and lateral surface for the first building in the array can lead to larger discrepancies in the downstream flow field. These seemingly minor issues when considering a single cube can propagate and compound simulation errors downstream in arrays of cubes.

The results obtained with LES are in good agreement with the experimental data accounting for an experimental uncertainty of 5% for most of the surfaces. At the windward surface, a slight temperature difference in the middle of the surface is observed due to the inadequacy of the single value for the Smagorinsky constant C_s when analyzing flow fields with impingement, separation, and free shear layers [46]. Differences in simulated and measured temperatures are also observed at the edge of the fifth cube and near its bottom. These disagreements are due to the low resolution of the infrared camera used to collect the temperatures at the cube edges and to the conductive heat loss from the heated cube to the base plate in the experiment [39].

In the present study, only the forced convection is taken into account. It should be noted that the cubes are actually mounted on a vertical wall in the experimental study under the assumption that the heat transfer is dominated by the forced convection [39]. The temperature difference between the two lateral surfaces is relatively small as shown in Fig. 4(b). Therefore, the local buoyancy effect is negligible and the forced convection dominates the local heat transfer to the surrounding fluid.

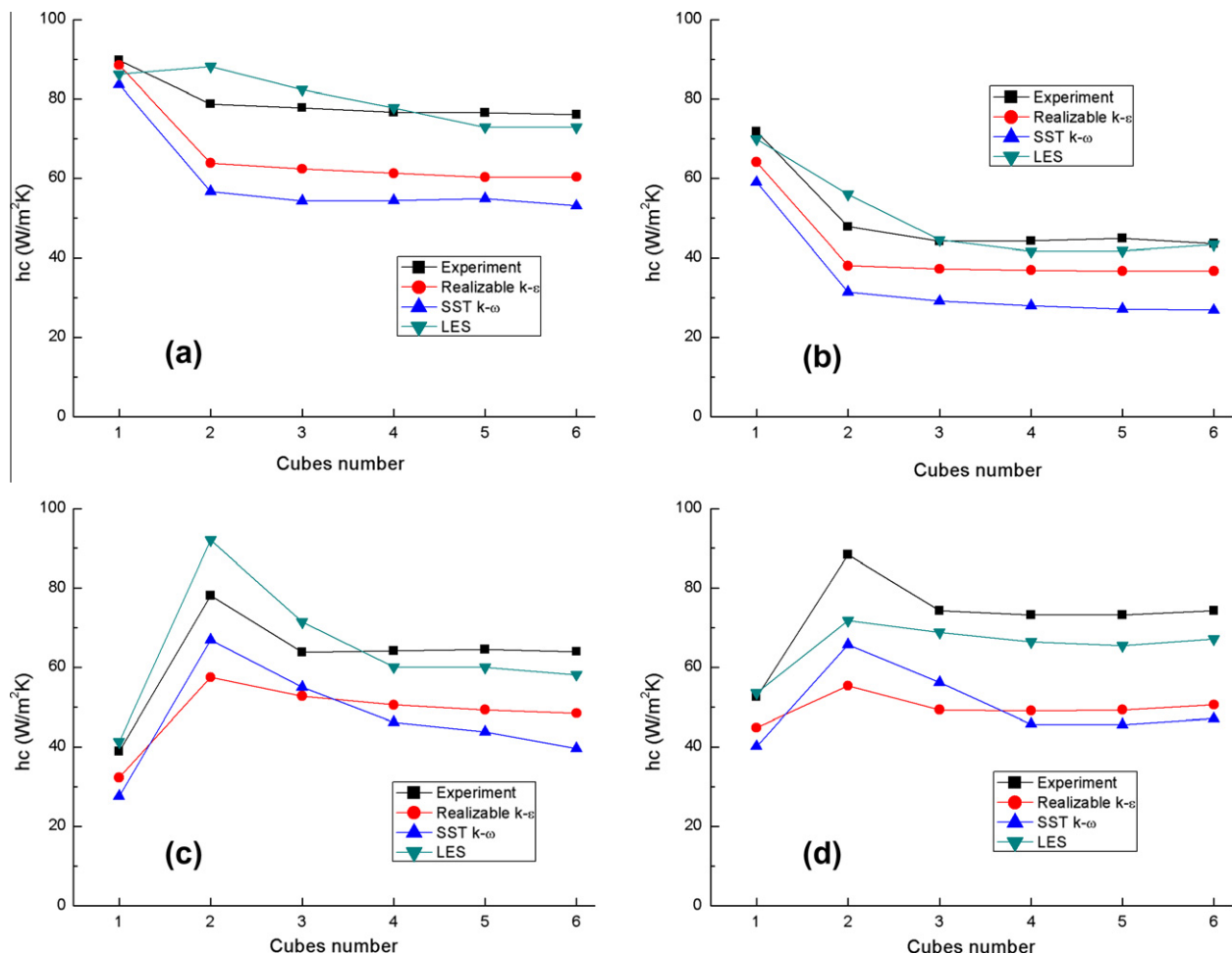


Fig. 5. The surface-averaged CHTC distribution obtained by CFD simulation and experiment on the first six cubes for the windward, leeward, lateral and top surfaces. (a) Windward surface, (b) leeward surface, (c) lateral surface and (d) top surface.

The surface-averaged CHTC is the major target of the current research work, which is calculated in CFD by the following equation:

$$h_{surf} = \frac{q_{conv}}{T_{surf} - T_{bulk}} \quad (12)$$

where q_{conv} is the convective heat flux, T_{surf} is the surface temperature and T_{bulk} is the bulk temperature.

The surface-averaged CHTC distribution for the first six cubes for windward, leeward, lateral and top surfaces, obtained from CFD simulations and experiments are presented in Fig. 5. The corresponding comparisons of the percentage difference between CFD results and experimental data are given in Fig. 6. The decay curve for surface-averaged CHTC is observed in windward and leeward surfaces by both experiments and RANS simulations. This effect is due to the impact of the reduced number and size of bounded vortices further downstream. Nevertheless, LES results show a lower CHTC in the first windward surface and a larger value in the second windward surface. These underestimated CHTCs are most likely due to the inaccurate simulation of the impinging region using the Smagorinsky–Lily model.

For the top and lateral surfaces, all of the RANS simulation results and experimental data have similar trends. For example, the flow separates at the front corners of the windward surface resulting in a wake region in the lateral and top surface of the first cube, while the flow downstream then attaches to the lateral and top surface of the second cube. Although RANS simulations can capture the main trends of the surface-averaged CHTC, the RANS simulation results are in some locations significantly different from the experimental data. Specifically, for the SST $k-\omega$ turbulence model, the differences in few locations are even more than 30% caused by the incapability to accurately predict flow field around arrays of cubes. The realizable $k-\varepsilon$ turbulence model results show slightly better performance with an averaged difference of approximately about 20%. However, the results still exhibit the limitations of RANS turbulence models.

The surface-averaged CHTC values for LES show a better agreement with the experimental data than any of the RANS models. It should be noted that the experimental data were obtained with an experimental uncertainty of less than 10% [39]. Therefore, the average difference of approximately 10% between the LES simulation results and experimental data is acceptable despite the local inaccuracies of up to 20%.

Overall, the numerical simulation results obtained with the SST $k-\omega$ turbulence model overpredict the surface temperatures up to 15% and significantly underpredict the surface-averaged CHTCs by

more than 30%. The realizable $k-\varepsilon$ turbulence in combination with the one-equation Wolfshtein model is not sufficiently accurate to estimate the CHTC in an array of cubes, though a good agreement with the experimental data for the windward surface is observed for the first cube in the present research and in an isolated cube in the existing studies [14,15]. LES with the Smagorinsky–Lily subgrid model provides relatively accurate results for CHTC in an array of cubes as long as sufficient computer resources are available. Therefore, in the present study, LES is carried out to determine flow field and convective heat transfer through arrays of buildings in the atmospheric boundary layer.

4. CFD simulation setup

The validation part of this investigation indicated that LES simulations with the Smagorinsky–Lily subgrid model can provide simulated CHTCs that are on average within 10% of the measured values. This model is then setup to provide CHTCs for new scenarios in urban environments to investigate influence of different flow regimes on the convective heat transfer. A special attention is devoted to the selection of domain geometry, boundary conditions, computational grids, and LES unsteady parameter settings.

4.1. Urban environments and domain geometry

To investigate surface heat transfer coefficients in different urban environments, a regular array of cubic buildings ($H = 10$ m), consisting of up to 14 rows, is modeled. Different plan area densities λ_p represented different urban environments and their corresponding flow regimes. According to the flow regimes determined by Oke [47], the present study identified three plan area densities to characterize skimming flow regime ($\lambda_p = 0.25$), wake interference flow regime ($\lambda_p = 0.11$), and isolated roughness flow regime ($\lambda_p = 0.04$). Furthermore, in an attempt to include the transition between flow regimes, two additional plan area densities ($\lambda_p = 0.16, 0.063$) are considered. Taking into account that higher plan area densities exist in city centers, another $\lambda_p = 0.44$ is also adopted. Overall, this study considered six different plan area densities ($\lambda_p = 0.04, 0.063, 0.11, 0.16, 0.25$, and 0.44) that are expected to result in different flow regimes to be further used for classification of urban environments with respect to convective heat transfer. It should be noted that this assumption for classification of urban environments is based on Oke's definitions of different flow regimes. In the past two decades, a number of studies have developed correlations between incoming wind and flow regimes, but most of them emphasized the relationship between the flow regimes and pollutant transport while neglecting thermal effects [48–50]. Therefore, the present study uses the flow regime classification, while taking into account the thermal transport in urban environments.

Table 2 presents detailed simulation case descriptions and simulation domain properties. In order to simulate fully developed turbulent flow and calculate CHTCs for various flow regimes in the streamwise direction, the size of simulation domains range from $21.5H$ to $23H$ and they include 5–14 rows of cubes. Due to the use of regular building arrays represented by cubes, the values of the plan area density λ_p and the frontal area density λ_f are the same. Different simulation scenarios have case names defined using the plan area density values, which are Case $\lambda_p[0.44]$, Case $\lambda_p[0.25]$, Case $\lambda_p[0.16]$, Case $\lambda_p[0.11]$, Case $\lambda_p[0.063]$ and Case $\lambda_p[0.04]$. Fig. 7 shows the layout of Case $\lambda_p[0.25]$. The origin of the Cartesian coordinate system is located at the intersection of the $X/H = 0$, $Y/H = 0$ and $Z/H = 0$ planes. Relative to the building array, the origin location is $1H$ upstream of the first building in the streamwise x direction, at the ground level in the vertical y

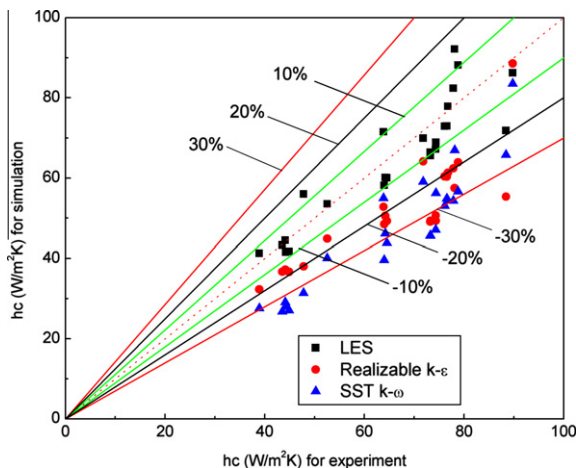


Fig. 6. Comparison of surface-averaged CHTC distributions between CFD simulation and experiment.

Table 2

Case description and simulation domain sizes.

Case	W/H	$\lambda_p(\lambda_f)$	Row number	Total domain length(L/H)
Case $\lambda_p[0.44]$	0.50	0.44	14	21.5
Case $\lambda_p[0.25]$	1.00	0.25	11	22
Case $\lambda_p[0.16]$	1.50	0.16	9	22
Case $\lambda_p[0.11]$	2.00	0.11	8	23
Case $\lambda_p[0.063]$	3.00	0.063	6	22
Case $\lambda_p[0.04]$	4.00	0.04	5	21

direction and in the center of the middle building row in the span-wise z direction.

4.2. Boundary conditions

In the atmospheric boundary layer, a mean wind velocity profile models the characteristic of the incoming wind. Therefore, at the inlet of the computational domain, the logarithmic wind profile is given as follows [14,15,51]:

$$\frac{U(z)}{u^*} = \frac{1}{\kappa} \ln \left(\frac{z+z_0}{z_0} \right) \quad (13)$$

where κ is the von Karman constant ($\kappa = 0.4$), u^* is the friction velocity, and z_0 is the roughness length. Due to the limitations of the Lettau relationship for estimating surface roughness in the regular arrays of elements [52], Macdonald et al. [30] provided an improved model. This improved model accounts for a non-linear relationship between the roughness height and plan area density as well as explicitly includes the obstacle drag coefficients. Therefore, based on this improved model for the estimation of surface roughness for obstacle arrays, z_0/H is obtained to generate the inlet velocity profiles shown in Table 3. Although the wind tunnel experiment is not conducted to provide sufficient details about the inlet boundary conditions, this improved model has been extensively used to model urban canopy flows [29,53,54]. In the present study,

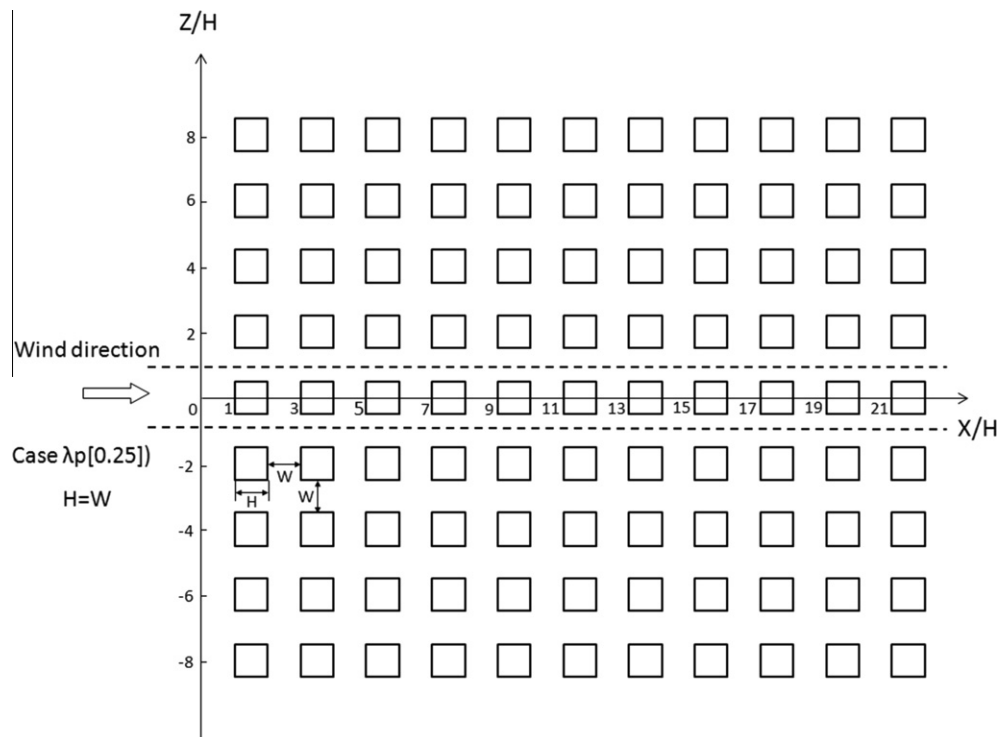
Table 3

Parameters for turbulent boundary layer.

Case	z_0/H	u^*/U_{10}
Case $\lambda_p[0.44]$	0.049	0.134
Case $\lambda_p[0.25]$	0.081	0.158
Case $\lambda_p[0.16]$	0.085	0.161
Case $\lambda_p[0.11]$	0.073	0.152
Case $\lambda_p[0.063]$	0.042	0.128
Case $\lambda_p[0.04]$	0.026	0.112

the mean wind speed at a height of 10 m above the ground, U_{10} , is set to 1 m/s, 3 m/s, 5 m/s and 7 m/s, resulting in the Reynolds number from 7×10^5 to 5×10^6 , based on H and U_{10} . The uniform temperature of 20 °C is specified as the inlet boundary condition.

To reduce the simulation domain size for Case $\lambda_p[0.25]$, the symmetry boundary conditions are applied at both sides of the simulation domain from $Z/H = -1$ to $Z/H = 1$, which is shown between the dotted lines in Fig. 7. Detailed descriptions of the computational domain and boundary conditions for Case $\lambda_p[0.25]$ are shown in Fig. 8. According to the recommendations from previous studies [40], a distance of $5H$ between the inflow boundary and the first building is required, and $15H$ between the outlet boundary and the last building of the domain is recommended. In addition, the domain features a distance of $5H$ between the lateral boundary and the closest lateral building wall, and $5H$ between the top boundary of the domain and the closest top surface of a building. In this study, the top surface of the domain is represented by the symmetry conditions. This particular boundary is typically defined as the slip wall or symmetry boundary [9,14,40]. The ground surface of the domain was adiabatic no-slip boundary with zero roughness. At the outlet boundary, outflow with zero gradient is imposed to generate a fully developed flow. All the external surfaces of buildings are assumed to be no-slip boundaries with zero roughness height and with an imposed constant temperature of 30 °C.

**Fig. 7.** Geometrical configuration for case $\lambda_p[0.25]$.

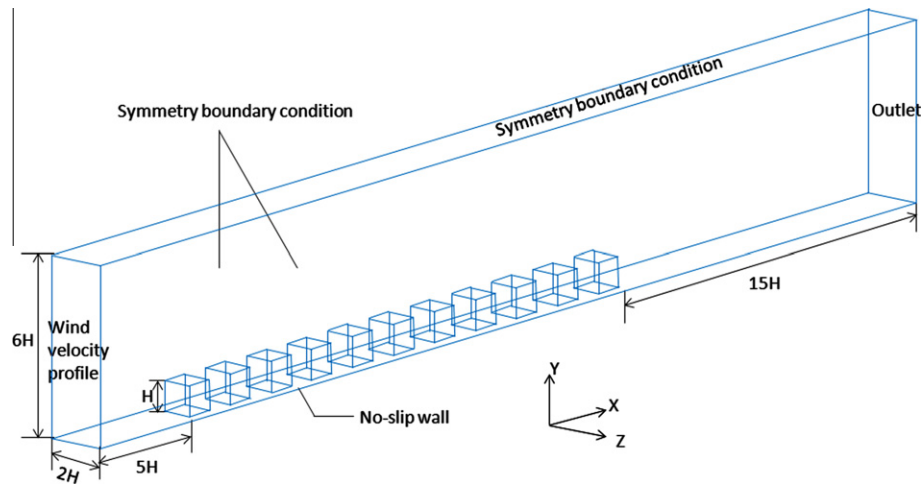


Fig. 8. Computational domain and boundary condition for Case $\lambda_p[0.25]$.

It should be noted that due to a relatively small Richardson number (Ri) calculated according to $U_{10} = 3$ m/s and 10°C temperature difference, the buoyancy effects are negligible. When the U_{10} velocity decreases to 1 m/s, the buoyancy effect starts having an influence on convective heat transfer, but it is still negligible. In addition, the radiation effects are also ignored. Therefore, this investigation only focuses on the forced convection.

4.3. Computational grids

In the LES simulations, one of the key considerations is the computational grid in the vicinity of the building surfaces, which require a high grid resolution for the near-wall treatment. Therefore, a small y^+ value ($y^+ \approx 1$) is required for wall-adjacent cells. A structured grid is employed in the entire computational domain. Fig. 9(a) shows the vertical cross-section of the computational grid distribution around one of the buildings. The building and the local computational zone are cubes as shown in Fig. 9(b), so the other cross-sections of this domain have the same sizes and grid numbers. Table 4 presents detailed grid information for each simulated case. To refine the grid close to the buildings, the maximum number of cells (7023,520) is utilized for Case $\lambda_p[0.11]$. It should be noticed that with the increase in U_{10} , the distance between the wall surfaces to the center of the first cell adjacent to the wall requires smaller values, so as to keep the value of y^+ ($y^+ \approx 1$) approximately constant. Therefore, for different U_{10} , an appropriate grid distribution adjacent to a wall is used to achieve $y^+ \approx 1$ in the majority of grids, except in the high velocity regions around cube edges where the maximal value of y^+ is up to 10. The averaged cell size in the wake between two cubes approximately changes from $0.15 \text{ m} \times 0.15 \text{ m} \times 0.25 \text{ m}$ (length \times width \times height) for Case $\lambda_p[0.44]$ to $0.40 \times 0.40 \times 0.25$ for Case $\lambda_p[0.04]$.

In this study, the grid independency evaluation is also carried out by changing grid numbers in the local computational zone around one building in all three directions. For different grid distributions, the results for GCI are compared for the reattachment length at the rooftop for the first building (X_R/H), as well as the Skin friction coefficient (C_f) and Nusselt number (Nu) for the windward surface of the third building. Here, Case $\lambda_p[0.25]$ with $U_{10} = 5$ m/s is taken as an example to summarize the grid independency results for three different grid distributions (coarse grid, Δ_1 : $40 \times 29 \times 40$, medium grid, Δ_2 : $48 \times 35 \times 48$, and fine grid, Δ_3 : $58 \times 42 \times 58$), shown in Table 5. It is found that the grid distribution of $48 \times 35 \times 48$ ($H \times W \times L$) shows good performance resulting in a grid independent flow around cubes. This grid

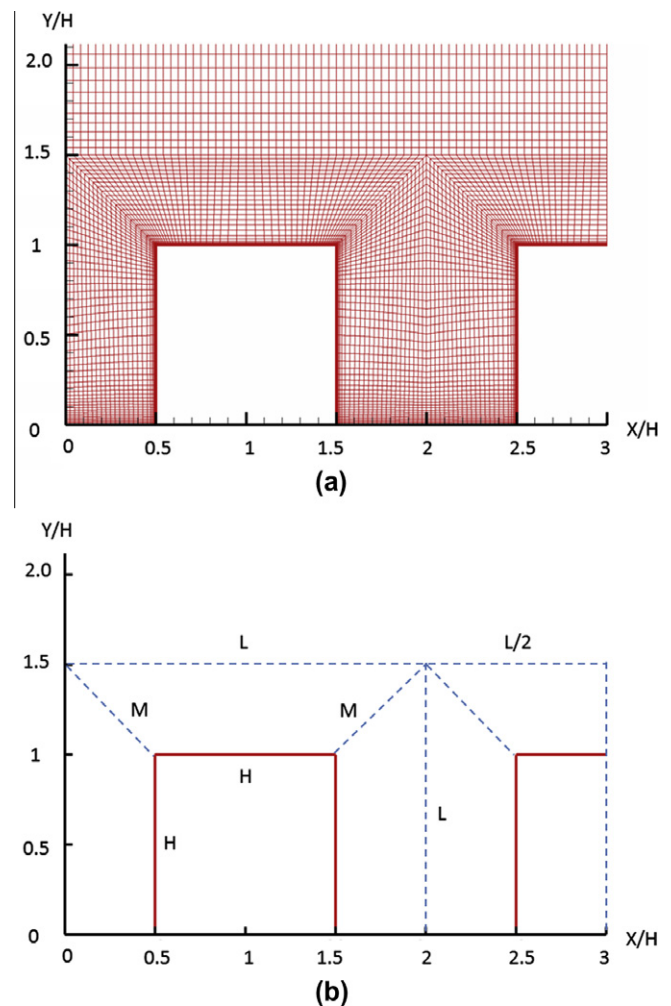


Fig. 9. The vertical cross-section of the computational zone around one of the buildings in Case $\lambda_p[0.25]$. (a) Grid distribution, (b) dimensions for local computational zone.

distribution provides a good compromise between the level of uncertainty and computational cost. The spatial discretization error is also estimated by the Richardson extrapolation, and is about 2.5% for Nusselt number (Nu) of 497 for the windward surface of the fifth cube.

Table 4

Detailed grid numbers for each case.

Case	Grid numbers in each divided zone around a building in three directions ($H \times M \times L$)	Total number of cells in the entire simulation domain
Case $\lambda_p[0.44]$	$44 \times 30 \times 44$	5853,100
Case $\lambda_p[0.25]$	$48 \times 35 \times 48$	6040,320
Case $\lambda_p[0.16]$	$52 \times 40 \times 52$	6407,080
Case $\lambda_p[0.11]$	$56 \times 45 \times 56$	7023,520
Case $\lambda_p[0.063]$	$60 \times 50 \times 60$	6603,000
Case $\lambda_p[0.04]$	$64 \times 55 \times 64$	6400,960

Table 5Grid convergence index (GCI) for Case $\lambda_p[0.25]$.

Grid numbers ($H \times W \times L$)	Reattachment length(X_R/H)	Skin friction coefficient (C_f)	Nusselt number (Nu)
GCI[2,1]	2.65%	15.7%	5.95%
GCI[3,2]	0.89%	2.84%	1.35%

 X_R/H : The reattachment length at the rooftop in first building. C_f and Nu : The average value based on the windward surface in third building.

4.4. Unsteady setting and parameters for LES

In order to capture a more realistic initial flow field for the LES runs and to reduce the initial duration needed for the LES simulation to obtain a statistically-steady solution, the first step is to obtain a steady-state solution by using a low Reynolds $k-\varepsilon$ turbulence model. The next step is to generate the instantaneous velocity field based on the low Reynolds $k-\varepsilon$ turbulence model results. Therefore, in order to obtain a steady-state solution using the low Reynolds $k-\varepsilon$ turbulence model, the turbulent kinetic energy (k) and the turbulent dissipation rates (ε) are first calculated by the following expressions:

$$k = \frac{u^*2}{0.3} \quad (14)$$

$$\varepsilon = \frac{u^*3}{\kappa(Z + Z_0)} \quad (15)$$

Afterwards, the initial duration for most of the runs is limited to $5T$ ($T = L/U_{10}$, where L is the domain size) to remove the influence of the initial condition, whereas an additional period of $10T$ is used to

provide the sufficient amount of data for the averaging of all the required parameters. For the Case $\lambda_p[0.25]$ with $U_{10} = 5$ m/s, the time step is set to $\Delta t = 0.02$ s, which ensures that the Courant–Friedrichs–Levy (CFL) number is always smaller than 1 in the majority of grid points, except in the region of high velocity around cube edges where the maximum values are at the range of 1.4–2.0. Correspondingly, the time steps for all other cases range from 0.01 s to 0.05 s according to different U_{10} for different cases. The number of iterations per time step is approximately 5–10 to obtain convergence at each time step. Finally, according to the validation case mentioned above, the time dependent boundary condition for inlet is also imposed by means of a vortex method with 190 vortices.

Given the importance of the turbulence intensity of the approaching wind flow to CHTC simulation results in the turbulent boundary layer [14], Fig. 10 presented the simulated mean streamwise velocity (U/U_{10}) and turbulence intensity (Ti) profiles at inlet ($X/H = -4$), and upstream of the first building ($X/H = -1$ and 0) in the building arrays for the Case $\lambda_p[0.44]$ with $U_{10} = 3$ m/s. The figure shows that the mean streamwise velocity profiles at the inlet, $X/H = -1$ and 0 are stable. The turbulence intensities at $X/H = -1$ and 0 show slight inconsistency with that at the inlet, but this is acceptable because of the flow impingement at the front building. For example, Blocken et al. [55] and Hargreaves et al. [56] reported the horizontal homogeneity problem at the atmospheric boundary layer; however, they focused on $k-\varepsilon$ turbulence models and standard wall functions. Therefore, for LES and near-wall treatment provided by Werner and Wengle, further studies are needed to examine horizontal homogeneity.

5. Results and discussions

The results for the specified urban environment simulation cases include flow field around arrays of buildings, surface-averaged CHTC distributions, and correlations for surface-averaged CHTC.

5.1. Flow field around arrays of buildings

The flow field is the first important result in establishing CHTCs for the six specified plan area densities. Fig. 11 presents the mean velocity contours and streamlines through the first two rows of buildings for $U_{10} = 5$ m/s in the vertical plane at the center of the domain. The flow field around the first building is characterized

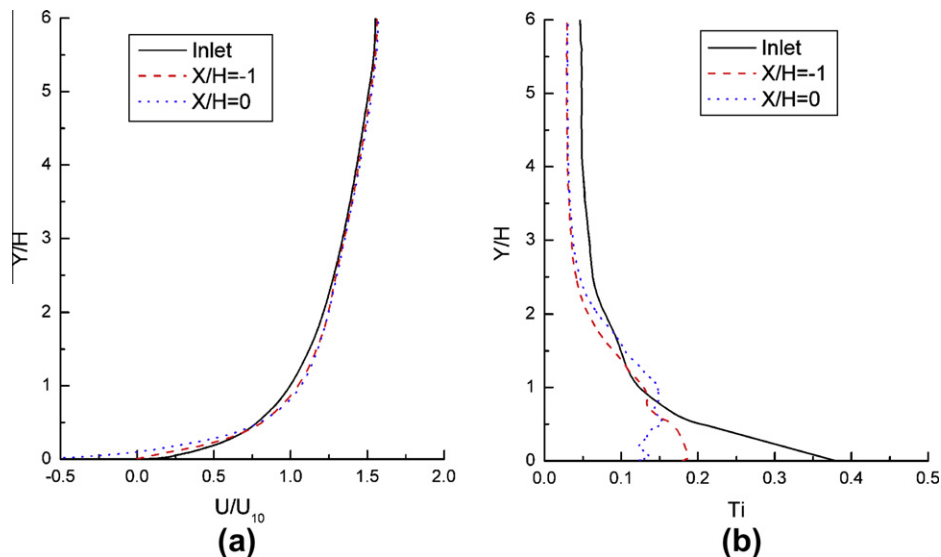


Fig. 10. Simulated mean streamwise velocity (U/U_{10}) and turbulence intensity (Ti) profiles at inlet ($X/H = -4$), and upstream of the first building ($X/H = -1$ and 0) in the building arrays for the Case $\lambda_p[0.44]$ with $U_{10} = 3$ m/s.

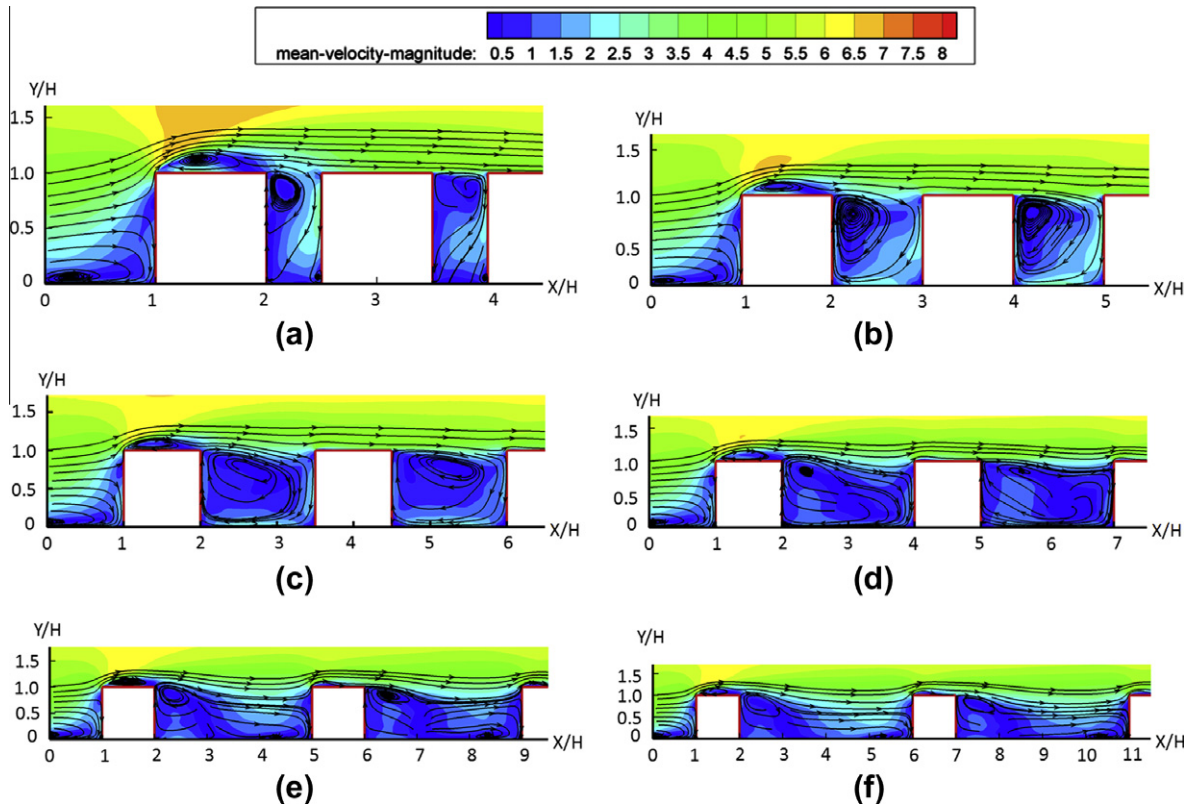


Fig. 11. Mean velocity contours and streamlines through the first two rows of buildings in the vertical plane at the center of the domain. (a) Mean velocity field for Case $\lambda_p[0.44]$, (b) mean velocity field for Case $\lambda_p[0.25]$, (c) mean velocity field for Case $\lambda_p[0.16]$, (d) mean velocity field for Case $\lambda_p[0.11]$, (e) mean velocity field for Case $\lambda_p[0.063]$ and (f) mean velocity field for Case $\lambda_p[0.04]$.

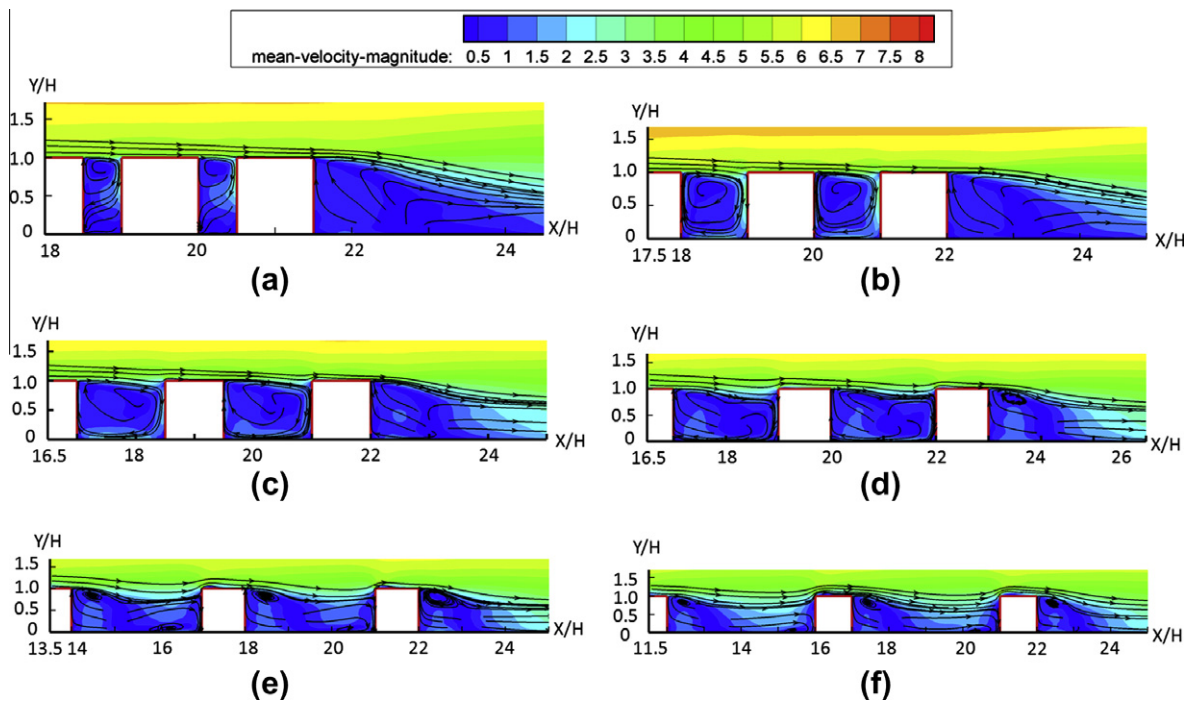


Fig. 12. Mean velocity contours and streamlines through the last two rows of buildings in the vertical plane at the center of the domain. (a) Mean velocity field for Case $\lambda_p[0.44]$, (b) mean velocity field for Case $\lambda_p[0.25]$, (c) mean velocity field for Case $\lambda_p[0.16]$, (d) mean velocity field for Case $\lambda_p[0.11]$, (e) mean velocity field for Case $\lambda_p[0.063]$ and (f) mean velocity field for Case $\lambda_p[0.04]$.

by impingement, separation, reattachment and recirculation. Similarly, Fig. 12 shows the mean velocity contours and streamlines through the last two rows of buildings for $U_{10} = 5$ m/s in the verti-

cal plane at the center of the domain. These flow fields are obtained to estimate how the convective heat transfer varies with different flow regimes.

It should be pointed that the different flow regimes were defined for street canyons [47], and not for arrays of buildings. In this study, only the flow fields at the center vertical plane of the domain were analyzed to explain the CHTC distribution for arrays of buildings. The modeled streamlines shown in Fig. 11(a) (Case $\lambda_p[0.44]$), and Fig. 11(b) (Case $\lambda_p[0.25]$) represent typical skimming flow characterized by a clear vortex circulation. Relatively high velocity magnitude is caused by the descending flow against the downstream building. Unfortunately, the flow transition regime from the skimming regime to the wake interference flow regime is not expected to occur in Case $\lambda_p[0.16]$. Thereby, the expected case sequence for matchup with flow regimes is incorrect and the further research requires one more case between Case $\lambda_p[0.25]$ and Case $\lambda_p[0.16]$ to investigate transition from the skimming regime to the wake interference flow regime. However, the focus of the current study is on the convective heat transfer coefficients. The missing flow regime does not affect the CHTC distribution that changes gradually with the plan area densities.

For Case $\lambda_p[0.16]$ shown in Fig. 11(c), a reverse horizontal flow appearance in the lower part of the building arrays is monitored, which is a feature of a wake interference. In addition, a decrease in velocity magnitude in the center of the building arrays is also predicted. Compared with the skimming flow, a small and weak vortex circulation behind the upwind building is observed.

Case $\lambda_p[0.11]$ shown in Fig. 11(d) presents a transition regime from the wake interference flow regime to the isolated roughness

flow regime, which is characterized by a small vortex occurrence behind the upwind building and a distinguished change in the velocity direction produced in the center of the building arrays. Furthermore, the streamlines close to the downstream building reveal that the flow horizontally impinges on the downstream building and then reverses in the lower part of the building arrays.

Cases $\lambda_p[0.063]$ and Cases $\lambda_p[0.04]$ are shown in Fig. 11(e) and (f), respectively. Both of these cases are characterized by the isolated roughness flow regime even though the original assumption was that different plan area densities represented different urban environments and flow regimes. Accordingly, similar flow characteristics appear at the recirculation behind the upstream building. In Case $\lambda_p[0.04]$, the flow field at the windward surface of the downstream building turns into a logarithmic profile. In other words, the vortex close to the upstream building represents a forward-directional flow with a logarithmic velocity profile. Specifically, this phenomena was observed in Case $\lambda_p[0.04]$, while in Case $\lambda_p[0.063]$ the spacing between the two buildings is not sufficiently large enough for the downstream building to encounter a well-defined logarithmic velocity profile.

In the last two rows of buildings shown in Fig. 12, the flow fields in the building arrays exhibits the same flow features as discussed above. However, for flow field behind the last row of buildings, there is no appearance of a dominant recirculation in Case $\lambda_p[0.44]$, Case $\lambda_p[0.25]$ and Case $\lambda_p[0.16]$ when compared with Case $\lambda_p[0.11]$, Case $\lambda_p[0.063]$ and Case $\lambda_p[0.04]$.

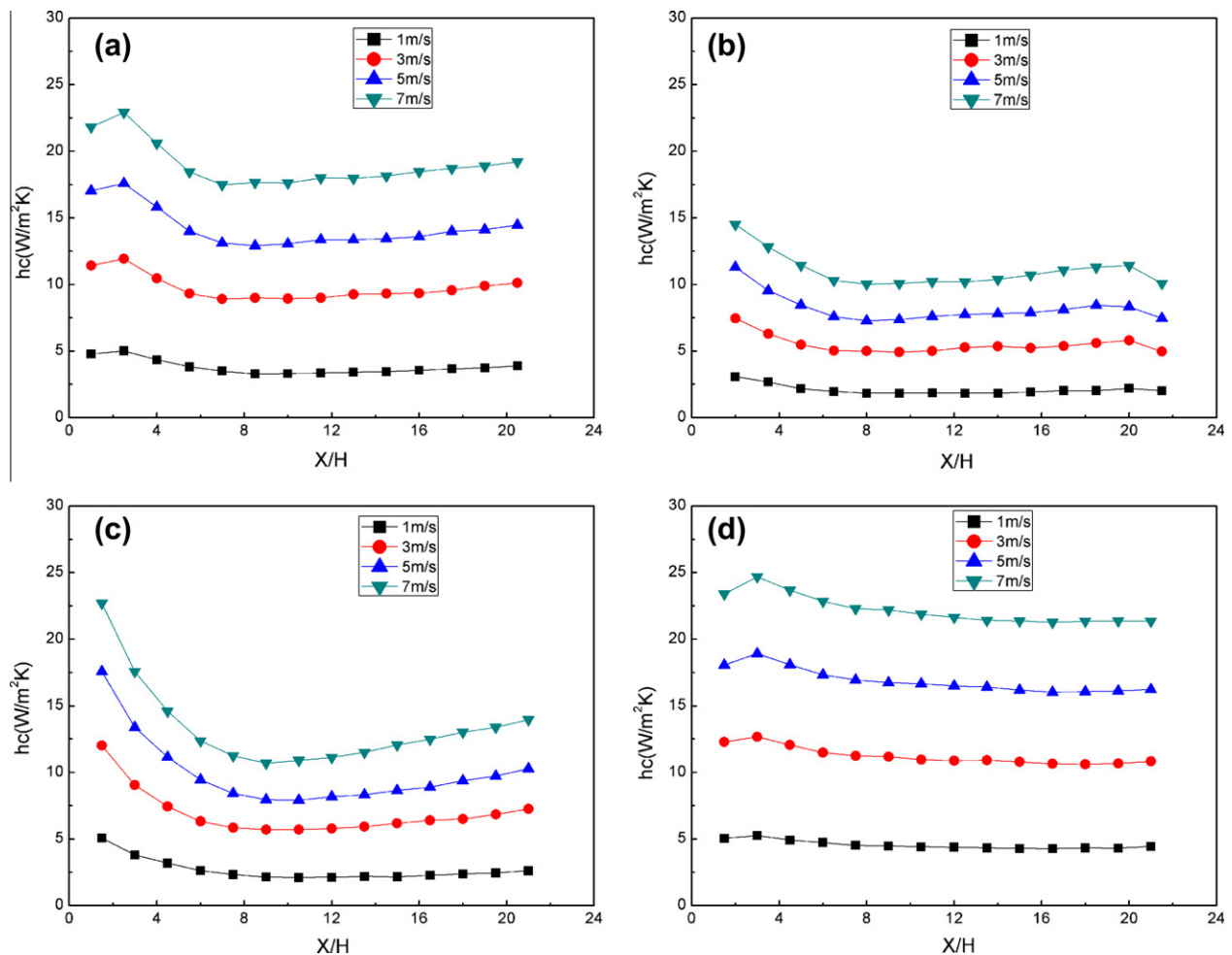


Fig. 13. The CHTC distributions for Case $\lambda_p[0.44]$ along x -axis direction. (a) Windward surface, (b) leeward surface, (c) lateral surface and (d) top surface.

5.2. Surface-averaged CHTC distributions

It is important to notice that in this subsection all references to CHTC indicate averaged-surface CHTC, unless otherwise specified. Figs. 13–15 show the CHTC distributions for Cases $\lambda_p[0.44]$, $\lambda_p[0.25]$, and $\lambda_p[0.16]$, respectively, for different incoming wind velocities including $U_{10} = 1$ m/s, 3 m/s, 5 m/s and 7 m/s. The figures show that most of the CHTC distributions have a decreasing trend along the x -axis, aligned with the incoming wind direction, for both the skimming and the wake interference flow regimes. This decrease in CHTCs is due to the loss of momentum that results from the impingement on the windward surface of the upstream buildings, resulting in vortices at the top and lateral surfaces of the upstream building, and weaker flow around the downstream buildings. Nevertheless, there are a few exceptions explained below:

- (1) A lower CHTC in the first windward surface and larger values in the two windward surfaces downstream are observed, which is probably attributed to the shortcoming of using the Smagorinsky–Lily model. As pointed out in the existing studies [46], it is not realistic to have one single value for C_s (0.1 selected in this study) to model various types of flow regimes around bluff bodies, such as impingement, separation and recirculation.
- (2) At the top surfaces, a similar pattern appears for CHTC values as described for the first windward surface. This pattern for the top surface is due to a bounded vortex that enveloped the top of the first cube and resulted in lower CHTC due to

the separating flow regime. Moreover, the downstream flow attaches at the top of the second row cube and causes an increase in the CHTC value. Therefore, in this case, it is the flow characteristic around bluff bodies that causes increase in CHTC downstream.

- (3) Some CHTCs significantly increase at the leeward and lateral surfaces of buildings in the downstream buildings, even exceeding the CHTC for some windward surfaces, such as the lateral surface in Case $\lambda_p[0.44]$. In this case, the building layout is characterized by narrower building arrays that drive wind out of building arrays more quickly than wider canyons present in other simulated cases. Fig. 16 shows a relatively larger horizontal velocity magnitudes inside of building arrays next to the lateral building surfaces, which is a flow feature also observed by Hang et al. [24].
- (4) A sudden drop in CHTC values for leeward surfaces in the last row of buildings is observed. Looking at the flow field around these rows of buildings shown in Fig. 12, the decrease in CHTC values could be due to the absence of a well-defined recirculation region. This wake recirculation decreases local velocities in the vicinity of the leeward surfaces, and its absence affects CHTC values.

It is shown that CHTC distributions for different incoming wind velocities U_{10} have a similar decay curve shape. Specifically, with the decrease of the plan area densities, the magnitude of the decay along the x -axis, aligned with the incoming wind direction, becomes weaker. Therefore, the simulation results for Cases

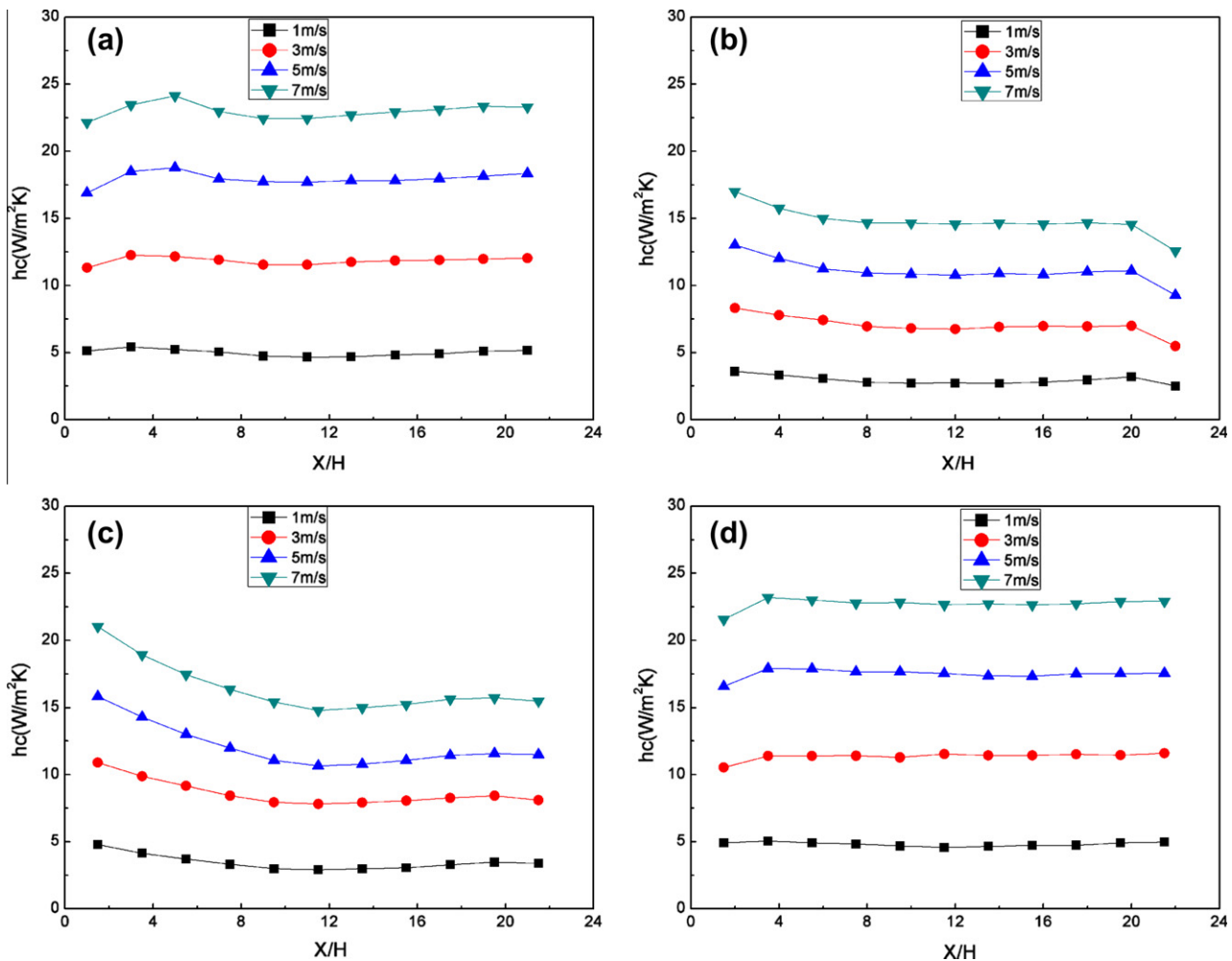


Fig. 14. The CHTC distributions for Case $\lambda_p[0.25]$ along x -axis direction. (a) Windward surface, (b) leeward surface, (c) lateral surface and (d) top surface.

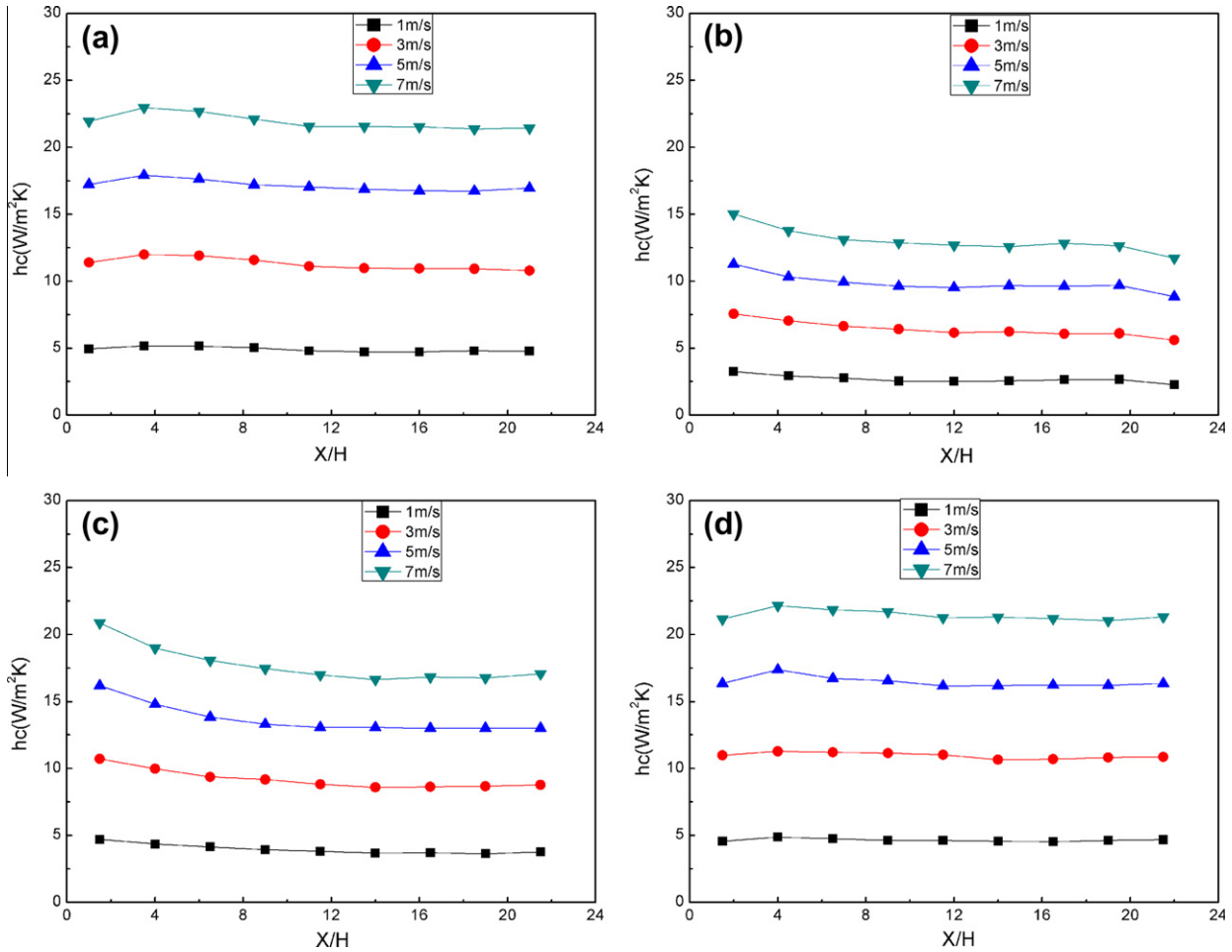


Fig. 15. The CHTC distributions for Case $\lambda_p[0.16]$ along x -axis direction. (a) Windward surface, (b) leeward surface, (c) lateral surface and (d) top surface.

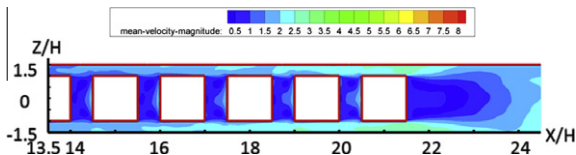


Fig. 16. Horizontal velocity magnitudes along x -axis direction for Case $\lambda_p[0.44]$.

$\lambda_p[0.11]$, Case $\lambda_p[0.063]$ and Case $\lambda_p[0.04]$ are very similar to the three cases for larger urban densities (0.44, 0.25, and 0.16) presented in Figs. 13–15. Furthermore, the simulation results for all six urban densities λ_p are used to compare CHTC values for the incoming wind velocity of $U_{10} = 5$ m/s.

Fig. 17 shows the numerical results for CHTC along an x -axis direction, at the windward, leeward, lateral and top surfaces with $U_{10} = 5$ m/s for different λ_p . Note that due to special CHTC distributions occurred from Case $\lambda_p[0.44]$ compared to other cases, they might be due to the fact that buoyancy effect starts having a significant influence on convective heat transfer in the narrower building array and will not be discussed in more detail below. In addition, Case $\lambda_p[0.44]$ will not be used to derive the CHTC correlations for different λ_p in Section 5.3.

For the windward surfaces, the CHTC values, shown in Fig. 17(a), decrease from Case $\lambda_p[0.25]$ to Case $\lambda_p[0.04]$, with the averaged CHTC values from $18.3 \text{ W/m}^2 \text{ K}$ to $15.8 \text{ W/m}^2 \text{ K}$. This trend is present because the greater a building array's width results in a weaker descending flow induced by the circulation behind an

upstream building. At the leeward surfaces, similar changes for CHTC values are also observed from Case $\lambda_p[0.25]$ to Case $\lambda_p[0.04]$ that are presented in Fig. 17(b). However, both Case $\lambda_p[0.04]$ and Case $\lambda_p[0.063]$ have approximately uniform CHTC values. This asymptotic trend for CHTC values is due to relatively small changes in the recirculation behind the upstream buildings for the isolated roughness flow with increasing the building array's width.

For the lateral surface, the CHTC values in Case $\lambda_p[0.04]$ become smaller than that in Case $\lambda_p[0.063]$ as shown in Fig. 17(c). This decrease in the CHTC values is due to the development of a horseshoe vortex around what now appears to be isolated buildings. At the top surfaces, CHTC values, presented in Fig. 17(d), are of similar magnitude for Case $\lambda_p[0.16]$, Case $\lambda_p[0.11]$ and Case $\lambda_p[0.063]$, whereas, Case $\lambda_p[0.25]$ have higher value and Case $\lambda_p[0.04]$ have lower value than those three cases. The values in Case $\lambda_p[0.25]$ can be attributed to no vortex separation at the first top surface and strong forward horizontal flow skimming the top surfaces of downstream buildings. The values in Case $\lambda_p[0.04]$ are most likely related to the development of separation and reattachment of flow regimes, resulting in a weak flow at the top surfaces of buildings.

5.3. Correlations for surface-averaged CHTC

In general, the CHTC values, obtained by running LES simulations, are correlated with the bulk wind speed, U_H , for windward, leeward, lateral and top surfaces. Power law correlations between CHTC and U_{10} have been widely used, so the present investigation first uses this relationship as well. For specific $\lambda_p = 0.25$, Fig. 18 dis-

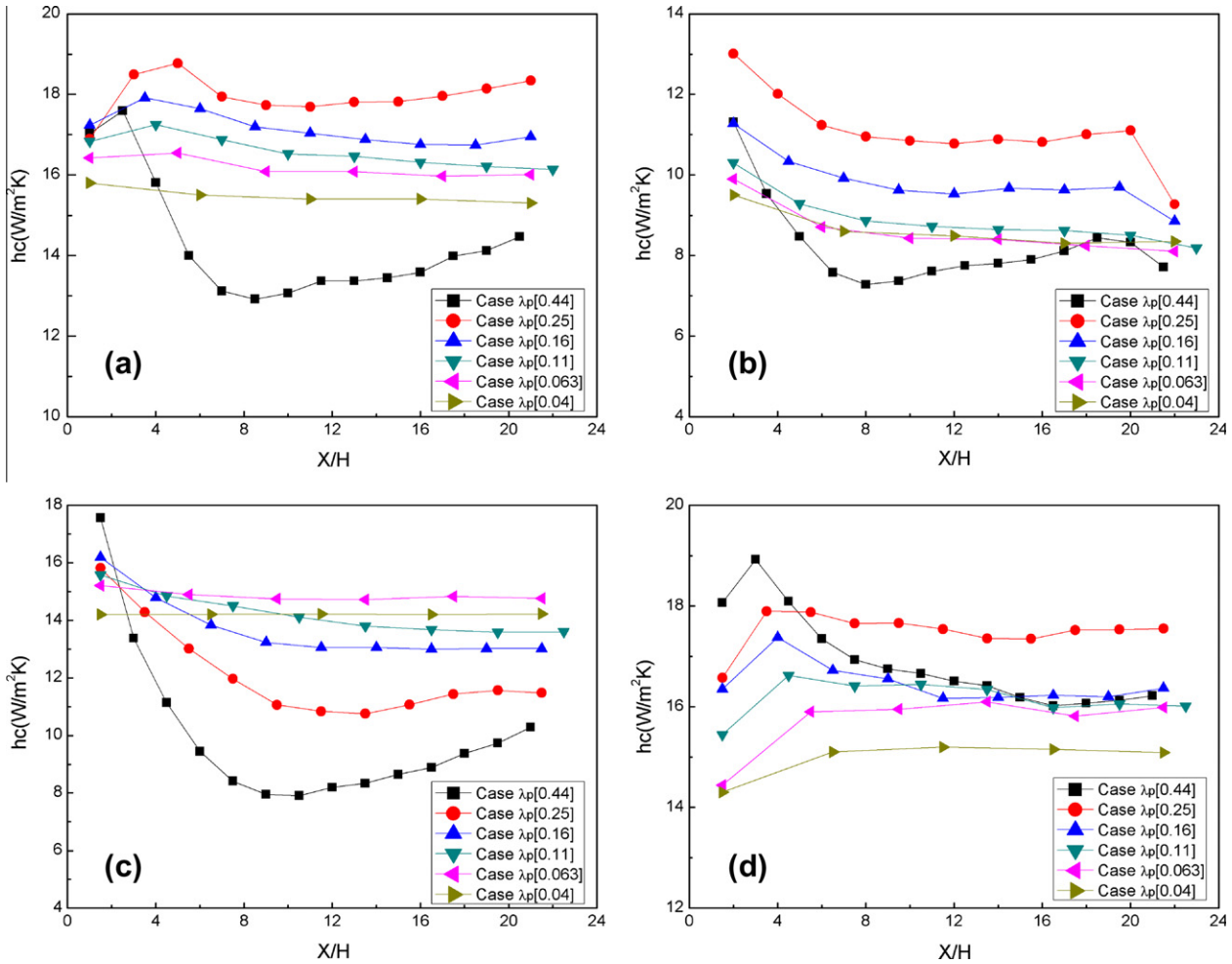


Fig. 17. Numerical results of CHTC along x-axis direction, on the windward, leeward, lateral and top surfaces at $U_{10} = 5$ m/s for different λ_p . (a) Windward surface, (b) leeward surface, (c) lateral surface and (d) top surface.

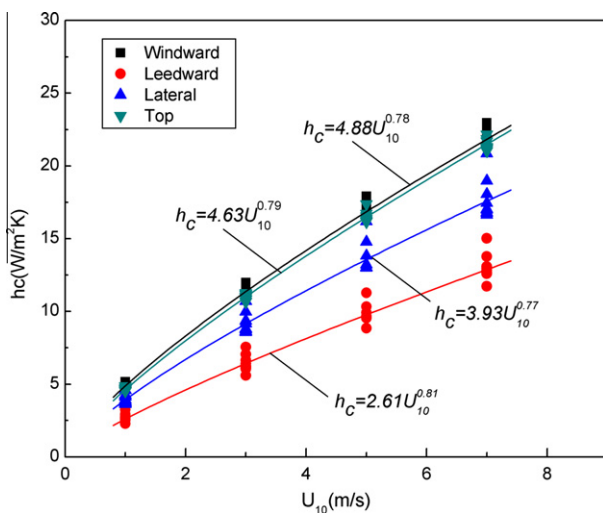


Fig. 18. CHTC as a function of U_{10} (≥ 1 m/s) for the windward, leeward, lateral and top surfaces at Case $\lambda_p[0.16]$.

plays the surface-averaged CHTC as a function of U_{10} (≥ 1 m/s) for windward, leeward, lateral and top surfaces. It shows a good curve fit as the coefficient of determination (R^2) is no less than 0.96.

Table 6

Convective heat transfer coefficients (h_c) correlations combined λ_p and U_{10} for isolated building and arrays of buildings.

Surface	h_c for isolated building ($\lambda_p = 0$) ^a	h_c for arrays of buildings $0.04 \leq \lambda_p \leq 0.25$
Windward	$3.88U_{10}^{0.82}$ ($R^2 = 0.99$)	$(4.45 + 2.42\lambda_p)U_{10}^{0.78}$ ($R^2 = 0.91$)
Leeward	$2.09U_{10}^{0.79}$ ($R^2 = 0.99$)	$(2.36 + 1.71\lambda_p)U_{10}^{0.79}$ ($R^2 = 0.90$)
Lateral	$3.45U_{10}^{0.82}$ ($R^2 = 0.99$)	$(4.39 - 3.33\lambda_p)U_{10}^{0.78}$ ($R^2 = 0.88$)
Top	$3.67U_{10}^{0.81}$ ($R^2 = 0.99$)	$(4.32 + 1.86\lambda_p)U_{10}^{0.79}$ ($R^2 = 0.90$)

^a Based on $z_0 = 0.03$ for the land surface coverage with lower grass and isolated obstacles.

In addition, this study uses the plan area density (λ_p) to define CHTC correlations expressed as follows:

$$h_c = (a + b\lambda_p)U_{10}^c \quad (16)$$

where a , b and c are two coefficients and an exponent, respectively. Note that Case $\lambda_p[0.44]$ is not included in the correlation since a relatively small R^2 is obtained. Table 6 shows the values of correlation coefficients for different λ_p and U_{10} , where λ_p varies from 0.04 to 0.25 and the Reynolds number ranges from 7×10^5 to 5×10^6 .

According to the simulation results, a decrease in λ_p results in the decrease of CHTCs for the windward, leeward and top surfaces. This influence of λ_p on the CHTCs is also confirmed by the weaker descending airflow behind the upstream buildings. For lateral sur-

faces, however, the CHTCs actually increase with the decrease of the plan area densities λ_p . This inverse relationship is attributed to the gradual development of a horseshoe vortex with the greater building array's widths. Therefore, with the increase of the plan area densities, CHTCs increase in the windward, leeward and top surfaces and decreases in the lateral surfaces, by up to 11%, 15%, 10% and 16%, respectively.

In order to evaluate CHTC results for smaller λ_p (<0.04), Table 6 presents the surface-averaged CHTC for isolated building ($\lambda_p = 0$) as a function of U_{10} (from 1 m/s to 7 m/s) for windward, leeward, lateral and top surfaces. The roughness length (z_0) is given as 0.03 [14], which indicates the land surface with lower grass and isolated buildings. Based on the results in Table 6, the CHTCs for isolated buildings are approximately 10–15% larger than the CHTCs obtained from the expressions for arrays of buildings when λ_p is equal to 0. This issue can be explained by the fact that the turbulent kinetic energy, which is determined by different roughness lengths z_0 , also plays an important role in calculating the CHTC values. Specifically, Blocken et al. [14] also reported that the 10% difference of incident turbulence intensity can result in up to 60% difference of surface-averaged CHTCs for an isolated building. Therefore, for smaller λ_p (<0.04), the CHTC calculations require input on roughness length. In the case of building array simulations, as the ones conducted in the present study, CHTCs are not as sensitive to the roughness lengths as the immediate building surroundings modulate the local turbulence intensities.

To investigate whether CHTC values are affected by the turbulence intensity of the approaching flow, Fig. 19 shows correlations between CHTCs and surface-averaged square root of turbulence kinetic energy ($k^{0.5}$) at the distance of 0.3 m upstream from the windward surface for all simulated cases. These CHTC correlations have higher R^2 than the correlations based on U_{10} and λ_p . Therefore, this local parameter is a good predictor of the convective heat transfer at the windward surface of a building. However, when deriving CHTC correlations based on $k^{0.5}$ for the leeward or top surfaces, a relatively small R^2 is obtained when compared to R^2 for the windward surface. This is mainly due to the presence of recirculation and separation at these surfaces, resulting in a different distribution of surface CHTC for the same incoming turbulence kinetic energy. Due to the interest in CHTCs that can be easily deployed in the total energy balance for buildings, the present study used incoming wind velocities and neighborhood urban densities as correlation parameters for CHTCs.

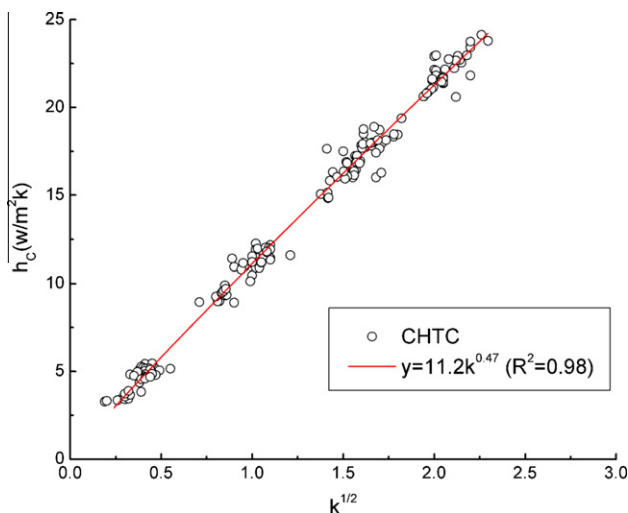


Fig. 19. The correlations between CHTCs and surface-averaged $k^{0.5}$ at the distance of 0.3 m upstream in the windward surface for all simulated cases.

Even though the present study focused on urban neighborhoods, the CHTC results for a single building are important. The CHTCs results for a single building can be directly compared to the findings in the present study for a limited case when urban density is equal to zero. Several previous studies [9,14,15] have presented CFD results of the surface-averaged CHTCs as a function of U_{10} for isolated buildings. These existing studies mainly focused on the windward surface and provided the following expressions $h_c = 5.14U_{10}^{0.82}$ for U_{10} of 0.05–5 m/s [14], $h_c = 4.6U_{10}^{0.89}$ for U_{10} of 1–4 m/s [15], and $h_c = 5.01U_{10}^{0.85}$ for U_{10} of 0.15–7.5 m/s [9]. The focus was on the windward surface because a strong agreement between the RANS simulations and experimental data was observed for isolated cubes. When comparing the existing findings to the CHTC results for an isolated building in the present study, these existing CHTCs at specific U_{10} for the windward surface are larger than the ones in Table 6, which is consistent with our finding that RANS over predicts the values of CHTC. Furthermore, these differences can also be attributed to the inlet boundary conditions selected in these cases, including turbulence intensity and a method used to generate instantaneous velocities at the inlet boundary for our LES simulations. As a result, future studies should carefully report the inlet boundary conditions for both numerical and experimental studies.

Last but not least, the current study neglected the buoyancy effect and only focused on the forced convective heat transfer because the flow regime was dominated by the forced convection. Nevertheless, for a different flow regime that would have a large value for the Richardson number ($Ri = Gr/Re^2$, where Gr is the Grashof number), the buoyancy force cannot be neglected as discussed in the existing literature [57]. Specifically, for the validation case in the current study, the value of the Reynolds number ($Re = 5066$) is relatively high when compared to the value of the Richardson number ($Ri = 0.001$), so the buoyancy induced convective heat transfer is negligible. Further, for the simulations of building arrays in Case $\lambda_p[0.25]$, the value of the Reynolds number ($Re = 7 \times 10^5$) indicates a turbulent flow regime, and the Richardson number value indicates a mixed convection ($Ri \approx 3$), but the buoyancy effect on CHTC was still negligible. For example, the buoyancy induced convective heat transfer with the incoming wind velocity of $U_{10} = 1$ m/s and temperature difference between the incoming wind temperature and local wall surface temperature of 10°C has a negligible effect on calculated CHTC as shown in Fig. 14. In other words, for the studied environmental conditions, the convective heat transfer at the surfaces of buildings in the array was not significantly altered by the presence of the buoyancy force. Therefore, the simulation results for Case $\lambda_p[0.25]$ with the incoming wind of $U_{10} = 1$ m/s are reliable for the purpose of defining CHTC shown in Table 6, even though the buoyancy force was neglected. Nevertheless, in a case of a mixed convective heat transfer regime, affected by both wind and buoyancy ($0.1 < Ri < 10$), the buoyancy force can change even the flow pattern around a building [58]. The flow motion induced by the buoyancy force can either strengthen or weaken the recirculation in between buildings and modify the recirculation structure, which further can result in a second counter-rotating vortex for higher values of Richardson number (Ri) [48,59,60]. In future studies, accounting for the combined effect of wind and buoyancy convective heat transfer at external building surfaces will be investigated in more detail.

6. Conclusions

In the present study, convective heat transfer coefficients (CHTC) at the external windward, leeward, lateral and top surfaces of building arrays immersed in a turbulent boundary layer were examined. This study used LES with the Smagorinsky–Lily model

to predict CHTC values, and then compared the simulation results with experimental data. It should be noted that a slight temperature difference in the middle of the surface was observed due to the shortcoming of using a constant value of C_s in the Smagorinsky–Lily model. In addition, steady RANS including the realizable $k-\varepsilon$ and the SST $k-\omega$ turbulence models were also used to compare with the experimental data. However, both of these RANS models underpredict CHTC values for building arrays in contrast to LES simulation results. Therefore, using validated LES, different flow fields were investigated for six different plan area densities λ_p and four different incoming wind velocities U_{10} , which produced the skimming, wake interference and isolated roughness flow regimes.

CHTC distributions for different λ_p and U_{10} are compared with flow characteristics in building arrays. From the high (0.44) to low (0.04) plan area densities, a decreasing trend in CHTCs is present at windward and leeward surfaces because the greater building arrays' widths result in a weaker descending flow induced by the circulation behind the upstream buildings. However, due to the building layout characterized by narrower building arrays, some CHTC distributions at lateral surfaces in Case $\lambda_p[0.44]$ and Case $\lambda_p[0.25]$ show an increasing trend for CHTCs in the last rows of buildings. In addition, a lower CHTC in the first windward surface and larger values in the downstream and two windward surfaces are also observed, which is attributed to the shortcomings of using the Smagorinsky–Lily model. Further studies could apply more complex subgrid models, such as the Dynamic Smagorinsky model, or Direct Numerical Simulation (DNS), to try to improve accuracy of calculated CHTCs. Finally, CHTC distributions were derived in the form of the power law correlations with U_{10} and λ_p . Specifically, for a constant incoming wind velocity U_{10} , with the increase of the plan area densities λ_p from 0.04 to 0.25, CHTCs increases 15% for the leeward surface and decreases 16% for the lateral surfaces. Overall, these correlations indicate that the density of urban neighborhoods directly affects the total energy balance at building surfaces, and, therefore, the associated building energy consumption.

Acknowledgements

This study is partially sponsored by the EFRI-1038264 award from the National Science Foundation (NSF), Division of Emerging Frontiers in Research and Innovation (EFRI). The study is also partially supported by the Fundamental Research Funds for the Central Universities in China (Grant No. SWJTU09ZT09).

Reference

- [1] J.A. Palyvos, A survey of wind convection coefficient correlations for building envelope energy systems' modeling, *Appl. Therm. Eng.* 28 (8–9) (2008) 801–808.
- [2] J.D. Spitler, C.O. Pedersen, D.E. Fisher, Interior convective heat transfer in buildings with large ventilative flow rates, *ASHRAE Trans.* 97 (1991) 505–515.
- [3] D.E. Fisher, C.O. Pedersen, Convective heat transfer in building energy and thermal load calculations, *ASHRAE Trans.* 103 (2) (1997) 137–148.
- [4] I. Beausoleil-Morrison, An algorithm for calculating convection coefficients for internal building surfaces for the case of mixed flow in rooms, *Energ. Build.* 33 (4) (2001) 351–361.
- [5] N.E. Wijesundera, B.R. Chou, S.E.G. Jayamaha, Heat flow through walls under transient rain conditions, *J. Build. Phys.* 17 (1) (1993) 118–141.
- [6] R. Chandra, V.K. Goel, B.C. Raychaudhuri, Universal curves for natural-convection heat-transfer coefficients in flat-plate solar-energy collectors, *Appl. Energ.* 13 (2) (1983) 101–107.
- [7] T. Ayata, P.C. Tabares-Velasco, J. Srebric, An investigation of sensible heat fluxes at a green roof in a laboratory setup, *Build. Environ.* 46 (9) (2011) 1851–1861.
- [8] H. Takebayashi, M. Moriyama, Surface heat budget on green roof and high reflection roof for mitigation of urban heat island, *Build. Environ.* 42 (8) (2007) 2971–2979.
- [9] T. Defraeye, B. Blocken, J. Carmeliet, Convective heat transfer coefficients for exterior building surfaces: existing correlations and CFD modelling, *Energ. Convers. Manage.* 52 (1) (2011) 512–522.
- [10] H. Nakamura, T. Igarashi, T. Tsutsui, Fluid flow and local heat transfer around two cubes arranged in tandem on a flat plate turbulent boundary layer, *JSME Int. J. B-Fluid T* 44 (4) (2001) 584–591.
- [11] H. Nakamura, T. Igarashi, T. Tsutsui, Local heat transfer around a wall-mounted cube at 45 degrees to flow in a turbulent boundary layer, *Int. J. Heat Fluid Fl.* 24 (6) (2003) 807–815.
- [12] K.C. Wang, R.T. Chiou, Local mass/heat transfer from a wall-mounted block in rectangular channel flow, *Heat Mass Transfer* 42 (7) (2006) 660–670.
- [13] M.G. Emmel, M.O. Abadie, N. Mendes, New external convective heat transfer coefficient correlations for isolated low-rise buildings, *Energ. Build.* 39 (3) (2007) 335–342.
- [14] B. Blocken, T. Defraeye, D. Derome, J. Carmeliet, High-resolution CFD simulations for forced convective heat transfer coefficients at the facade of a low-rise building, *Build. Environ.* 44 (12) (2009) 2396–2412.
- [15] T. Defraeye, B. Blocken, J. Carmeliet, CFD analysis of convective heat transfer at the surfaces of a cube immersed in a turbulent boundary layer, *Int. J. Heat Mass Transfer* 53 (1–3) (2010) 297–308.
- [16] T. Defraeye, J. Carmeliet, A methodology to assess the influence of local wind conditions and building orientation on the convective heat transfer at building surfaces, *Environ. Modell. Softw.* 25 (12) (2010) 1813–1824.
- [17] S. Sharples, Full-scale measurements of convective energy-losses from exterior building surfaces, *Build. Environ.* 19 (1) (1984) 31–39.
- [18] D.L. Loveday, A.H. Taki, Convective heat transfer coefficients at a plane surface on a full-scale building facade, *Int. J. Heat Mass Transfer* 39 (8) (1996) 1729–1742.
- [19] A. Hagishima, J. Tanimoto, Field measurements for estimating the convective heat transfer coefficient at building surfaces, *Build. Environ.* 38 (7) (2003) 873–881.
- [20] R.D. Clear, L. Gartland, F.C. Winkelmann, An empirical correlation for the outside convective air-film coefficient for horizontal roofs, *Energ. Build.* 35 (8) (2003) 797–811.
- [21] Y. Liu, D.J. Harris, Full-scale measurements of convective coefficient on external surface of a low-rise building in sheltered conditions, *Build. Environ.* 42 (7) (2007) 2718–2736.
- [22] J.T. Shao, J. Liu, J.N. Zhao, W.W. Zhang, D.X. Sun, Z.P. Fu, A novel method for full-scale measurement of the external convective heat transfer coefficient for building horizontal roof, *Energ. Build.* 41 (8) (2009) 840–847.
- [23] S. Saneinejad, P. Moonen, T. Defraeye, J. Carmeliet, Analysis of convective heat and mass transfer at the vertical walls of a street canyon, *J. Wind Eng. Ind. Aerod.* 99 (4) (2011) 424–433.
- [24] J. Hang, Y.G. Li, M. Sandberg, L. Claesson, Wind conditions and ventilation in high-rise long street models, *Build. Environ.* 45 (6) (2010) 1353–1365.
- [25] K. Narita, Wind tunnel experiment on convective transfer coefficient in urban street canyon, in: *Proceedings of the fifth International Conference on Urban Climate*, Lodz, Poland, 2003, pp. 355–358.
- [26] I.S. Walker, D.J. Wilson, Wind Shadow Model for Air Infiltration Sheltering by Upwind Obstacles, *Hvac&R Res.* 2 (4) (1996) 265–282.
- [27] G.E. Mattingly, E.F. Peters, Wind and trees – air infiltration effects on energy in housing, *J. Ind. Aerodynam.* 2 (1) (1977) 1–19.
- [28] B.J. Burley, Infiltration mapping for urban environments: PhD thesis, The Pennsylvania State University, University Park, PA; 2007.
- [29] R.W. Macdonald, Modelling the mean velocity profile in the urban canopy layer, *Bound. Lay. Meteorol.* 97 (1) (2000) 25–45.
- [30] R.W. Macdonald, R.F. Griffiths, D.J. Hall, An improved method for the estimation of surface roughness of obstacle arrays, *Atmos. Environ.* 32 (11) (1998) 1857–1864.
- [31] T.H. Shih, W.W. Liou, A. Shabbir, Z.G. Yang, J. Zhu, A new kappa-epsilon Eddy viscosity model for high Reynolds-number turbulent flows, *Comput. Fluids* 24 (3) (1995) 227–238.
- [32] F.R. Menter, 2-Equation Eddy-viscosity turbulence models for engineering applications, *AIAA J.* 32 (8) (1994) 1598–1605.
- [33] D.K. Lilly, A proposed modification of the Germano-Subgrid-Scale closure method, *Phys. Fluids A-Fluid* 4 (3) (1992) 633–635.
- [34] E.R. Seo, A numerical study of buoyant turbulent flows using Low-Reynolds number $k-\varepsilon$ model: PhD thesis, Texas Tech University, Texas, US; 2001.
- [35] M. Wolfshtein, Velocity and temperature distribution in one-dimensional flow with turbulence augmentation and pressure gradient, *Int. J. Heat Mass Transfer* 12 (3) (1969) 301–308.
- [36] ANSYS Fluent 12 Theory Guide, US: ANSYS Inc; April 2009.
- [37] H. Werner, H. Wengle, Large-Eddy simulation of turbulent flow over and around a cube in a plate channel, in: *The eighth symposium on turbulent shear flows*, Munich, Germany, 1991.
- [38] E.R. Meinders, T.H. vanderMeer, K. Hanjalic, C.J.M. Lasance, Application of infrared thermography to the evaluation of local convective heat transfer on arrays of cubical protrusions, *Int. J. Heat Fluid Fl.* 18 (1) (1997) 152–159.
- [39] E.R. Meinders, Experimental study of heat transfer in turbulent flows over wall-mounted cubes: PhD thesis, Technische Universiteit Delft, Delft, The Netherlands; 1998.
- [40] J. Franke, A. Hellsten, H. Schellen, B. Carrissimo, Best practice guideline for the CFD simulation of flows in the urban environment, COST Action 732: Quality assurance and improvement of microscale meteorological models, Hamburg, 2007.
- [41] P.J. Roache, Verification and validation in computational science and engineering, Hermosa Publishers, New Mexico, 1998.
- [42] P.J. Roache, Perspective – a method for uniform reporting of grid refinement studies, *J. Fluid Eng.-T. ASME* 116 (3) (1994) 405–413.

- [43] P. Gousseau, B. Blocken, G.J.F. van Heijst, CFD simulation of pollutant dispersion around isolated buildings: on the role of convective and turbulent mass fluxes in the prediction accuracy, *J. Hazard. Mater.* 194 (2011) 422–434.
- [44] P. Gousseau, B. Blocken, T. Stathopoulos, G.J.F. van Heijst, CFD simulation of near-field pollutant dispersion on a high-resolution grid: a case study by LES and RANS for a building group in downtown Montreal, *Atmos. Environ.* 45 (2) (2011) 428–438.
- [45] F. Mathey, D. Cokljat, J.P. Bertoglio, E. Sergent, Assessment of the vortex method for large eddy simulation inlet conditions, *Prog. Comput. Fluid Dy.* 6 (1–3) (2006) 58–67.
- [46] S. Murakami, Overview of turbulence models applied in CWE-1997, *J. Wind Eng. Ind. Aerod.* 74 (6) (1998) 1–24.
- [47] T.R. Oke, Street design and urban canopy layer climate, *Energ. Build.* 11 (1–3) (1988) 103–113.
- [48] X.X. Li, C.H. Liu, D.Y.C. Leung, K.M. Lam, Recent progress in CFD modelling of wind field and pollutant transport in street canyons, *Atmos. Environ.* 40 (29) (2006) 5640–5658.
- [49] C.H. Liu, M.C. Barth, D.Y.C. Leung, Large-eddy simulation of flow and pollutant transport in street canyons of different building-height-to-street-width ratios, *J. Appl. Meteorol.* 43 (10) (2004) 1410–1424.
- [50] I. Eliasson, B. Offerle, C.S.B. Grimmond, S. Lindqvist, Wind fields and turbulence statistics in an urban street canyon, *Atmos. Environ.* 40 (1) (2006) 1–16.
- [51] B. Blocken, T. Stathopoulos, P. Saathoff, X. Wang, Numerical evaluation of pollutant dispersion in the built environment: comparisons between models and experiments, *J. Wind Eng. Ind. Aerod.* 96 (10–11) (2008) 1817–1831.
- [52] H. Lettau, Note on aerodynamic roughness-parameter estimation on the basis of roughness-element description, *J. Appl. Meteorol.* 8 (1969) 828–832.
- [53] D. Hamlyn, R. Britter, A numerical study of the flow field and exchange processes within a canopy of urban-type roughness, *Atmos. Environ.* 39 (18) (2005) 3243–3254.
- [54] S. Di Sabatino, E. Solazzo, P. Paradisi, R. Britter, A simple model for spatially-averaged wind profiles within and above an urban canopy, *Bound-Lay. Meteorol.* 127 (1) (2008) 131–151.
- [55] B. Blocken, T. Stathopoulos, J. Carmeliet, CFD simulation of the atmospheric boundary layer: wall function problems, *Atmos. Environ.* 41 (2) (2007) 238–252.
- [56] D.M. Hargreaves, N.G. Wright, On the use of the k -epsilon model in commercial CFD software to model the neutral atmospheric boundary layer, *J. Wind Eng. Ind. Aerod.* 95 (5) (2007) 355–369.
- [57] J. Gryzagoridis, Combined free and forced-convection from an isothermal vertical plate, *Int. J. Heat Mass Transfer* 18 (7–8) (1975) 911–916.
- [58] B. Ruck, Wind-tunnel measurements of flow-field characteristics around a heated model-building, *J. Wind Eng. Ind. Aerod.* 50 (1–3) (1993) 139–152.
- [59] W.C. Cheng, C.H. Liu, D.Y.C. Leung, On the correlation of air and pollutant exchange for street canyons in combined wind-buoyancy-driven flow, *Atmos. Environ.* 43 (24) (2009) 3682–3690.
- [60] X.M. Xie, C.H. Liu, D.Y.C. Leung, Impact of building facades and ground heating on wind flow and pollutant transport in street canyons, *Atmos. Environ.* 41 (39) (2007) 9030–9049.